The motion of long drops in rectangular microchannels at low capillary numbers

Sai Sashankh Rao[1] and Harris Wong[1],†

[1]Department of Mechanical and Industrial Engineering, Louisiana State University, Baton Rouge, LA 70803, USA

Drop flow in rectangular microchannels has been utilized extensively in microfluidics. However, the pressure-gradient versus flow-rate relation is still not well understood. We study the motion of a long drop in a rectangular microchannel in the limit the capillary number $Ca \to 0$ ($Ca = \mu U/\sigma$, where U is the constant drop velocity, μ is the viscosity of the carrier liquid and σ is the interfacial tension). In this limit, the moving drop looks like the static drop and has two end caps connected by a long column, which is surrounded by thin films on the microchannel wall and by menisci along the microchannel corners. Integral axial force balances on the drop fluid and on the carrier liquid surrounding the drop relate the carrier-liquid pressure gradient to the drop-fluid pressure gradient and the contact-line drag. The contact-line drag is argued to be the same as that for a long bubble (which has been determined by Wong *et al.* (*J. Fluid Mech.*, vol. 292, 1995*b*, pp. 95–110)) if the viscosity ratio $\lambda \ll Ca^{-1/3}$ and $\lambda \ll L$, where $\lambda = \bar{\mu}/\mu$, $\bar{\mu}$ is the drop viscosity and L ($\gg 1$) is the dimensionless drop length. Thus, the force balances yield one equation relating the two pressure gradients. The two pressure gradients also drive unidirectional flows in the drop and in the corner channels along the long middle column. These coupled flows are solved by a finite-element method to yield another equation relating the two pressure gradients. From the two equations, we determine the pressure gradients and thus the unidirectional velocity fields inside and outside the drop for $\lambda = 0$–100 and various microchannel aspect ratios. We find that in the limit $LCa^{1/3} \to 0$, the contact-line drag dominates and the carrier liquid bypasses the drop through the corner channels alongside the drop. For $LCa^{1/3} \gg 1$, the contact-line drag is negligible and the corner fluid is stationary. Thus, the drop moves as a leaky piston. We extend our model to a train of long drops, and compare our model predictions with published experiments.

Key words: drops, microfluidics, multiphase flow

---

1. Introduction

Living organisms often involve large numbers, such as the tens of thousands of genes encoding the genome or the plethora of proteins regulating the expression of these genes or the millions of cells comprising a tissue microenvironment.

† Email address for correspondence: hwong@lsu.edu

To analyse such a large number of biomolecules or cells, it is essential to develop a reliable lab-on-a-chip technology based on droplet microfluidics (Stone, Stroock & Ajdari 2004; Huebner *et al.* 2008; Teh *et al.* 2008; Anna 2016). Droplets provide a convenient means to isolate individual biomolecules or cells, enabling single entity analysis. Furthermore, nearly identical droplets can be generated at rates of 1–10 kHz with volumes as low as picolitres, allowing millions of droplets to be produced in less than an hour for analysis. Droplets have also been applied in the pharmaceutical and fine chemical industries as individual nanovolume batch reactors. Microfluidic devices can be used to aid the quick determination of chemical stoichiokinetics, and heat and mass transfer parameters (Song, Chen & Ismagilov 2006; Baroud, Gallaire & Dangla 2010). Moreover, the ease of drop-size control leads to levels of mass transfer and reaction regulation otherwise unachievable in stirred batch reactors (Jovanović *et al.* 2010). Microreactors could also be the preferred choice for expensive and toxic reactants due to the small volume of the droplets. Furthermore, when the droplet velocity is known, the reaction time inside the droplet grows linearly with the distance moved by the droplet, making it easier to measure chemical kinetics (Sarrazin *et al.* 2006). Two-phase flows in microfluidic devices have also been successfully employed in creating emulsions that are commonly used in the chemical, textile and food industries, which require precise control of the drop size and the polydispersity (Tan *et al.* 2008).

Despite these compelling advantages of droplet-based microfluidics, fundamental challenges remain to transform current droplet-based devices to next-generation fluidic processors that are capable of characterizing the large-scale complexity inherent in biological and chemical systems. Currently, there is no rigorous model that predicts the relation between pressure gradient and flow rate for drop flow in rectangular microchannels, implying that the throughput of a device is unknown. Development of a rigorous model would improve our understanding of drop flow in microchannels, which might lead to better design of large-scale two-phase fluidic processors.

Although gas–liquid two-phase flows in capillaries have been modelled extensively (Vladimir & Homsy 2006), there are only a few studies on the flow patterns and pressure drop in liquid–liquid flows (Baroud *et al.* 2010). Early studies of the immiscible liquid–liquid flow patterns use predominantly circular tubes (Lac & Sherwood 2009; Soares & Thompson 2009; Jovanović *et al.* 2011). However, drop flow in rectangular microchannels is different from that in circular capillaries because the carrier liquid can bypass the drop through corner channels. The corner flow can alter the flow characteristics and pressure drop, as shown theoretically by Wong, Radke & Morris (1995*b*) in their study of the motion of long bubbles in polygonal capillaries.

Two-phase flow in rectangular microchannels has been investigated numerically using most commonly the volume of fluid method (Sarrazin *et al.* 2008; Cherlo, Kariveti & Pushpavanam 2010; Raj, Mathur & Buwa 2010; Yong *et al.* 2011; Hoang *et al.* 2013). While the numerical method is well suited for studying the motion of short drops ($L < 5$) moving at capillary number $Ca \approx 0.01$, it has been challenging to simulate the motion of longer drops moving at smaller capillary numbers. Long moving drops deposit thin films on the wall, the thickness of which varies with Ca. For most experimental systems, $Ca \ll 1$, and the thickness of the thin film is much smaller than the width of the capillary. Resolving the physics in this thin-film region is necessary to accurately capture the velocity and pressure fields. Furthermore, spurious currents can arise from inaccurate calculations of the curvature of the interface and must be suppressed. These numerical challenges make the simulation of long drops at low capillary numbers computationally expensive.

Here, we model the motion of long drops in rectangular microchannels at low capillary numbers. The microchannel geometry, drop velocity, and fluid physical properties are first labelled in §2 and then used to make all variables dimensionless. An integral force balance is performed on a column of carrier liquid enclosing the long moving drop in §2.1, and on the drop fluid in §2.2. The two integral force balances are combined in §2.3 to yield an equation relating the streamwise carrier-liquid pressure gradient to the drop-fluid pressure gradient and the contact-line drag. The previously derived contact-line drag for long bubbles can be applied to long drops if the drop viscosity is not too high (§2.4). Thus, the two constant pressure gradients are the only unknown parameters to be determined. The pressure gradients also drive streamwise flows inside and outside the drop, as described in §3. Since the drop is long, the drop-fluid and carrier-liquid flows can be taken as unidirectional and obey the Poisson equation. The carrier-liquid pressure gradient is eliminated using the integral-balance equation, and the only unknown parameter left is the drop-fluid pressure gradient. The streamwise velocities inside and outside the drop are expanded as linear functions of two parameters to extract their dependence explicitly, and the expansion coefficients are solved by a finite-element method in §4.1. These velocities are integrated over the cross-sectional areas of their respective flow domains to give the volume flow rates in §4.2. Since the drop volume flow rate is simply the drop velocity times the drop cross-sectional area, it is prescribed. Equating this prescribed flow rate to the numerically integrated value leads to a solution of the drop-fluid pressure gradient in §4.2. The carrier-liquid pressure gradient is then determined from the integral force balance in §4.3. The streamwise velocity fields inside and outside the drop are presented in §4.4. We apply these results in §5 to determine the pressure-velocity relation (§5.1), the coefficient of mobility (§5.2), the excess pressure gradient (§5.3), the velocity ratio for two drops of unequal lengths (§5.4), and the pressure gradient for a train of drops (§5.5). We compare with published experimental results in §6. We discuss the assumptions made in our model and some details in §7. The work is concluded in §8.

2. The problem definition

Consider a long Newtonian drop of length LW ($L \gg 1$) moving with constant velocity U in a rectangular microchannel of width $2W$ and height $2BW$, as shown in figure 1(*a*). The drop with viscosity $\bar{\mu}$ is carried by an immiscible Newtonian liquid with viscosity μ. The drop is surrounded by a clean interface with interfacial tension σ. We study the drop motion in the limit the capillary number Ca ($= \mu U / \sigma$) $\rightarrow 0$. In this limit, capillary forces dominate and the shape of the moving drop resembles that of the static drop; it has two end caps connected by a long column with approximately uniform cross-sections (Wong, Morris & Radke 1992). The carrier liquid is taken to be perfectly wetting so that the column is surrounded by thin liquid films on the microchannel wall and by liquid menisci along the microchannel corners (figure 1*b*). As the carrier liquid is driven through the microchannel by a pressure gradient, it can either push the drop (plug flow) or bypass the drop through the corner channels (corner flow). The main objective of this work is to determine the pressure-gradient versus flow-rate relation for the carrier liquid as it drives the drop to move at velocity U.

For the rest of this paper, all lengths are made dimensionless by W, areas by W^2, pressures by σ/W, streamwise pressure gradients by σ/W^2, velocities by σ/μ, volume flow rates by $\sigma W^2/\mu$, the contact-line drag by σW, the contact-line-drag density by σ/W^2, and the hydraulic resistances by μ/W^4. We use σ/μ as the velocity scale
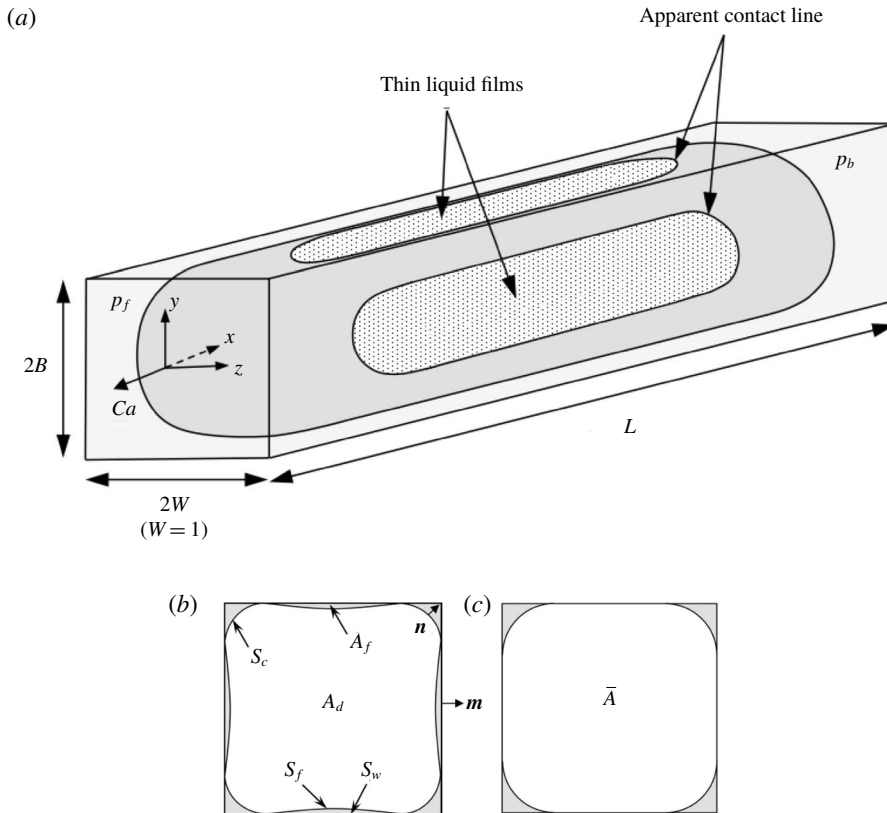
FIGURE 1. (*a*) Stationary control volume enclosing a non-wetting drop of dimensionless length L moving with steady dimensionless velocity Ca carried by a wetting liquid in a rectangular microchannel of width 2 and aspect ratio B ($\geqslant 1$) (the case of $B=1$ is shown). A dimensionless Cartesian coordinate system (x, y, z) is defined at the nose of the drop with x pointing downstream. The dimensionless carrier-liquid pressure p_b at the back end of the drop is higher than the pressure p_f at the front, and the difference drives the drop and can push the carrier liquid to bypass the drop through corner channels. (*b*) Cross-section of a moving long drop far from the ends. The drop (unshaded region with cross-sectional area A_d) is surrounded by the carrier liquid (shaded region) in thin films with cross-sectional area A_f and in corner channels. The film thickness has been exaggerated for clarity. The interface between the drop and the carrier liquid is separated into a corner part with area S_c and a film part with area S_f. The microchannel wall area covered by the thin films is denoted by S_w. The unit vectors **m** and **n** are normal to the wall and interface, respectively, and are pointing outwards. (*c*) Cross-section of a static long drop far from the ends. The bubble (unshaded region) has cross-sectional area $\bar{A}$.

because it is independent of whether the corner or plug flow dominates (see discussion in §7). After non-dimensionalization, the drop velocity becomes Ca, as shown in figure 1(*a*). All drop variables are denoted by an overbar, and all dimensional variables by an asterisk.

2.1. *An integral force balance on the carrier liquid surrounding the drop*

A stationary control volume is defined that encloses the moving drop and the carrier liquid at a particular instant in time, as shown in figure 1(*a*). Since the drop motion is

steady, the normal forces exerted on the carrier liquid at the two ends of the control volume must balance the streamwise shear forces on the sides of the control volume applied by the microchannel wall on the carrier liquid:

$$(p_b - p_f)A_T = \iint_{S_T} \nabla u \cdot \boldsymbol{m} \, \mathrm{d}S, \tag{2.1}$$

where p_f and p_b are the carrier-liquid pressures at the front and back ends of the drop, respectively. Because the drop is long $(L \gg 1)$, the variation in liquid pressure over each end plane is small compared with the pressure difference across the drop. Thus, p_f and p_b are treated as constant and $p_b > p_f$ (figure 1*a*). Normal viscous stresses on the end planes are of the same order as the liquid-pressure variation in the end regions, and are negligible compared with the pressure difference in (2.1). The area A_T $(= 4B)$ is the cross-sectional area of the rectangular microchannel. A Cartesian coordinate system (x, y, z) is defined at the nose of the drop with x pointing downstream (figure 1*a*). The streamwise velocity component is denoted by u and $\nabla = \boldsymbol{j}\partial/\partial y + \boldsymbol{k}\partial/\partial z$ is the two-dimensional gradient operator. The unit vector $\boldsymbol{m}$ is normal to the wall and points out of the control volume (figure 1*b*). The streamwise viscous shear stress is integrated over the sidewall area $S_T = 4(B + 1)L$ (figure 1*a*). Body forces such as inertia and gravity are neglected owing to the small size of the microchannel.

The drop is surrounded by thin liquid films and corner menisci. The thin films, once deposited by the front end, evolve slowly over a long streamwise length scale because their thickness $\sim Ca^{2/3}$ (Wong, Radke & Morris 1995*a*), and are therefore taken to maintain the same profile over the length of the drop (see § 7). The corner menisci are also assumed to have the same shape along the drop because the radius of interfacial curvature varies by $O(Ca^{2/3})$ along the drop (Wong *et al.* 1995*b*). We divide the control volume into a drop and a corner region, and study the forces on each control volume separately. The drop control volume consists of the drop and the thin films surrounding the drop. It is taken to be a right cylinder with uniform cross-sectional area $A_d + A_f$, where A_d and A_f are the cross-sectional areas of the moving drop and thin films, respectively, as shown in figure 1(*b*). An integral force balance on the drop control volume in the streamwise direction gives

$$(p_b - p_f)(A_d + A_f) = \iint_{S_c} \nabla u \cdot \boldsymbol{n} \, \mathrm{d}S + \iint_{S_w} \nabla u \cdot \boldsymbol{m} \, \mathrm{d}S. \tag{2.2}$$

The left-hand side is the pressure force driving the drop control volume, whereas the right-hand side is the total shear resistance. The first term of the shear resistance is the corner drag exerted on the drop by the carrier liquid flowing in the corner channels, where S_c represents the corner interfacial area. The unit vector $\boldsymbol{n}$ is normal to the interface and points outwards from the drop. The second term is the shear force on the drop exerted by the microchannel wall on the thin films surrounding the drop, where S_w represents the wall area in contact with the thin films. The wall shear stress peaks at the front and back ends of the drop near the curved contact lines, because the wetting carrier liquid experiences the largest shear stress as it squeezes into or out of the thin-film regions. These large shear forces at the two ends near the curved contact lines were called the contact-line drag (D_C) by Wong *et al.* (1995*b*) in their theoretical study of drag on long bubbles. Away from the contact-line regions, the shear stress is uniform across the thin films because the films are thin ($\sim Ca^{2/3}$) such

that the shear stress at the wall is maintained all the way to the interface. Thus, the wall shear stress in (2.2) can be written as

$$\iint_{S_w} \nabla u \cdot \boldsymbol{m} \, \mathrm{d}S = D_C + \iint_{S_f} \nabla u \cdot \boldsymbol{n} \, \mathrm{d}S, \tag{2.3}$$

where S_f represents the interfacial area between the drop and thin films, and the area integral over S_f is called the film drag. Substituting (2.3) into (2.2) gives the integral force balance as

$$(p_b - p_f)(A_d + A_f) = D_C + \iint_{S_f + S_c} \nabla u \cdot \boldsymbol{n} \, \mathrm{d}S. \tag{2.4}$$

Shear forces on the control surface at the end-cap regions are negligible compared with the listed shear forces because the cap regions are much shorter than the drop.

The corner control volume contains the corner channels shown in figure 1(*b*). Driven by the pressure difference, the carrier liquid flows through the corner channels subject to the no-slip condition at the wall and shear resistance at the corner interfaces. This corner flow will be studied in § 3.

2.2. *An integral force balance on the drop fluid*

Since the drop is moving at constant speed, the forces on the drop fluid must balance. An integral force balance in the streamwise direction on the drop fluid inside the drop surface gives

$$(\bar{p}_b - \bar{p}_f)A_d = \iint_{S_f + S_c} \lambda \nabla \bar{u} \cdot \boldsymbol{n} \, \mathrm{d}S, \tag{2.5}$$

where $\bar{p}_f$ and $\bar{p}_b$ are the drop-fluid pressures at, respectively, the front and back ends of the drop. These pressures can be treated as constant because $L \gg 1$ and the pressure variation within the end region is small compared with $(\bar{p}_b - \bar{p}_f)$. The right-hand side of (2.5) is the streamwise shear forces exerted by the carrier liquid on the drop at the thin-film interfacial area S_f (film drag) and the corner interfacial area S_c (corner drag), where $\lambda = \bar{\mu}/\mu$ is the viscosity ratio, and $\bar{u}$ is the *x*-component of the drop-fluid velocity (S_f and S_c are illustrated in figure 1*b*). The film drag always resists the motion of the drop because the film is thin and the microchannel wall is stationary. The corner drag will resist the drop motion if the carrier liquid in the corner channels moves slower than the drop. Thus, every part of the drop surface experiences a shear force opposing the drop motion. To balance these shear forces, the back pressure $\bar{p}_b$ must be higher than the front pressure $\bar{p}_f$. However, this pressure gradient can change direction if the carrier liquid in the corner channels moves from the back towards the front to bypass the drop. In that case, the corner drag reverses direction and points in the direction of the moving drop. Hence, when the corner flow dominates, the total streamwise shear force on the drop surface can point towards the front and consequently $\bar{p}_f > \bar{p}_b$ in (2.5). This pressure difference will drive the drop fluid along the drop centre from the front towards the back of the drop, opposite to the drop-moving direction. In the force balance (2.5), the drop is treated as a right cylinder with cross-sectional area A_d, as shown in figure 1(*b*). This is possible because $L \gg 1$ and the end-cap regions where the cross-sectional area differs from A_d are small compared with the length of the drop. Further, the contact-line drag does not appear because there is no length scale within the drop that is comparable to the thin-film thickness.

Aspect ratio	R	b_1	b_2	$\bar{A}$	C_D	k_s
$B = 1.0$	0.5302	0.4698	0.4698	3.759	13.35	1.778
$B = 1.2$	0.5780	0.4220	0.6220	4.513	14.92	1.254
$B = 1.5$	0.6346	0.3654	0.8654	5.654	17.89	0.8514
$B = 2.0$	0.7019	0.2981	1.298	7.577	23.87	0.5466

TABLE 1. Static drop dimensionless geometric parameters R, b_1, b_2 and $\bar{A}$, drag coefficient C_D and dimensionless hydraulic resistance k_s for various microchannel aspect ratio B. The geometric parameters are illustrated in figures 1(*c*) and 2, and are calculated from the analytic solutions derived by Wong *et al.* (1995*a*). The drag coefficient is introduced in (2.8), and the equation for k_s is given in (5.5*b*).

2.3. *Combination of the two integral force balances*

At the interface between the drop and the carrier liquid, a shear-stress balance in the streamwise direction gives

$$\nabla u \cdot \boldsymbol{n} = \lambda \nabla \bar{u} \cdot \boldsymbol{n}. \tag{2.6}$$

Substituting (2.6) into (2.5) and subsequent substitution into (2.4) yields

$$(p_b - p_f)\bar{A} = D_C + (\bar{p}_b - \bar{p}_f)\bar{A}, \tag{2.7}$$

where A_d and $(A_d + A_f)$ have been replaced by $\bar{A}$, which is the cross-sectional area of the static drop depicted in figure 1(*c*) because $A_d \sim 1$, and $(A_d - \bar{A})$ and A_f are $O(Ca^{2/3})$ (Wong *et al.* 1995*b*). The area $\bar{A}$ has been determined by Wong *et al.* (1995*b*) for various rectangular microchannels and is listed in table 1. Thus, the pressure force acting on the drop by the carrier liquid balances the contact-line drag and the pressure force on the drop fluid. In the next subsection, the contact-line drag D_C is studied.

2.4. *Contact-line drag*

The contact-line drag for long bubbles in polygonal capillaries has been solved by integrating the wall shear stress under the liquid film in the limit $Ca \to 0$ (Wong *et al.* 1995*b*):

$$D_C = C_D Ca^{2/3}, \tag{2.8}$$

where the drag coefficient C_D is a dimensionless constant that depends only on the capillary geometry. The values of C_D are listed in table 1 which are valid for $L \ll Ca^{-1}$. Within this bubble length, the deposited film does not rearrange (Wong *et al.* 1995*a*). The bubble contact-line drag holds also for drops if

$$\lambda \ll Ca^{-1/3}. \tag{2.9}$$

This is shown by the interfacial stress balance (2.6). Near the contact-line region, the dimensional film thickness $\sim Ca^{2/3}W$ (Hodges, Jensen & Rallison 2004). Hence, the dimensional shear stress within the thin film is $O[\mu U/(Ca^{2/3}W)]$. When the plug flow dominates, the drop-fluid velocity $\sim U$, and the largest dimensional shear stress within the drop is $O[\bar{\mu} U/(Ca^{1/3}W)]$, because the axial length scale $(Ca^{1/3}W)$ in the thin film induces a corresponding cross-stream (smallest) length scale in the drop

fluid (Hodges *et al.* 2004). Thus, the shear stress exerted by the drop fluid on the thin-film interface is negligible compared with the shear stress within the thin film if $\lambda \ll Ca^{-1/3}$. Therefore, the contact-line drag D_C obtained by Wong *et al.* (1995*b*) for long bubbles is applicable to our problem within this upper bound of viscosity ratio. Consequently, our contact-line drag is independent of drop viscosity. Park & Homsy (1984) studied two-phase flow in a Hele-Shaw cell and also find that the contact-line drag for a bubble holds for a drop if the viscosity ratio $\lambda \ll Ca^{-1/3}$. Hodges *et al.* (2004) analysed the thin film deposited by a long drop moving in a circular tube, and found that the film thickness is the same as that for a long bubble if $\lambda \ll Ca^{-1/3}$. (If the corner flow dominates, then the upper bound becomes $\lambda \ll L$, as derived in § 7.)

Substituting D_C from (2.8) into (2.7) gives

$$(p_b - p_f)\bar{A} = C_D Ca^{2/3} + (\bar{p}_b - \bar{p}_f)\bar{A}. \tag{2.10}$$

The contact-line drag is a positive constant. The second term on the right-hand side (the film and corner drags on the drop) is positive when the drop moves faster than the corner flow. However, it may become negative if the corner flow moves faster than the drop. No matter how negative it becomes, the magnitude can never exceed the contact-line drag because $p_b > p_f$ always.

3. Coupled streamwise flows

The pressure difference $(p_b - p_f)$ in the carrier liquid drives the liquid through the corner channels. The pressure difference $(\bar{p}_b - \bar{p}_f)$ in the drop fluid drives a streamwise flow inside the drop. The drop flow and the corner flow are coupled through boundary conditions at the corner interfaces. This coupling leads to another relation between $(p_b - p_f)$ and $(\bar{p}_b - \bar{p}_f)$ which, when combined with (2.10), will yield a solution for the pressure differences.

3.1. *Governing equations*

A long drop has an extended middle region with approximately uniform cross-sections, as shown in figure 1(*a*). The end regions where the cross-sectional area varies significantly have $O(1)$ length, which is much less than the length of the drop (Wong *et al.* 1992). Thus, the fluids inside and outside the drop move unidirectionally along the long middle region of the drop and obey

$$\nabla^2 u = P_x, \tag{3.1}$$

$$\nabla^2 \bar{u} = \frac{1}{\lambda}\bar{P}_x, \tag{3.2}$$

where

$$P_x = \frac{(p_b - p_f)}{L}, \quad \bar{P}_x = \frac{(\bar{p}_b - \bar{p}_f)}{L}, \tag{3.3a,b}$$

are streamwise pressure gradients. The integral force balance (2.10) can be written as

$$P_x = D + \bar{P}_x, \tag{3.4}$$

where
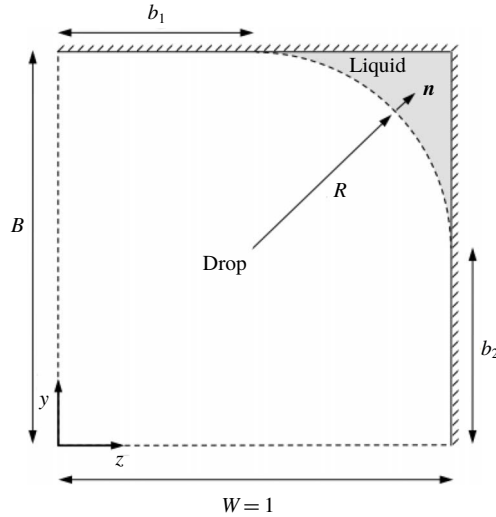
$$D = \frac{C_D}{\bar{A}}\frac{Ca^{2/3}}{L}, \tag{3.5}$$

FIGURE 2. Unit cell of the static long drop in figure 1(c). The rectangular microchannel has half-width W $(= 1)$ and aspect ratio B $(\geqslant 1)$. The carrier liquid (shaded region) is perfectly wetting, resulting in zero contact angle between the interface and the microchannel wall. The radius of curvature of the corner interface is denoted by R and the unwetted wall lengths are denoted by b_1 and b_2, respectively. Analytic solutions of these geometric parameters have been derived by Wong *et al.* (1995*a*), and their values are listed in table 1 for $B = 1$, 1.2, 1.5 and 2. The unit vector $\boldsymbol{n}$ is normal to the interface and points outwards.

is the dimensionless contact-line drag per unit drop volume and is called the contact-line-drag density for the rest of the paper. From (2.10), D is a positive constant, $\bar{P}_x$ may be positive or negative, and P_x is always positive. The carrier-liquid pressure gradient P_x is substituted into (3.1) to yield

$$\nabla^2 u = D + \bar{P}_x. \tag{3.6}$$

Thus, $\bar{P}_x$ is the only unknown parameter to be determined. For the rest of this paper, we will use D and $\bar{P}_x$ as driving forces for corner flow with the understanding that each represents a part of P_x.

3.2. *Boundary conditions*

The fluid-flow domains are shown in figure 2, which depicts a unit cell of the static drop graphed in figure 1(c). The radius of curvature of the static interface is denoted by R and the unwetted wall lengths are denoted by b_1 and b_2, respectively. Analytic solutions of these geometric parameters have been derived using an axial integral force balance by Wong *et al.* (1995*a*), and their values are listed in table 1 for rectangular microchannels of aspect ratio $B = 1$, 1.2, 1.5 and 2. At the corner interface shown in figure 2, the velocities are continuous:

$$u = \bar{u} \tag{3.7}$$

and the streamwise shear stresses are balanced:

$$\nabla u \cdot \boldsymbol{n} = \lambda \nabla \bar{u} \cdot \boldsymbol{n}, \tag{3.8}$$

where n is a unit vector normal to the interface as shown in figure 2. This shear-stress balance assumes a clean interface. The normal stress balance yields the static interface shape in the limit of zero capillary number. Furthermore, the carrier liquid and the drop fluid obey the no-slip condition at the wall:

$$u = \bar{u} = 0. \tag{3.9}$$

The drop-fluid velocity $\bar{u}$ has zero normal gradient at the symmetry planes of the unit cell shown in figure 2.

3.3. *Volume-flow-rate equations*

Since the immiscible drop is a closed system, the streamwise volume flow rate at each cross-sectional plane of the long middle column of the drop must equal the plug-flow rate of the drop. Thus, the drop volume flow rate is

$$\bar{Q} = \iint_{\bar{A}} \bar{u} \, dy \, dz = -\bar{A} Ca. \tag{3.10}$$

This integral constraint will determine $\bar{P}_x$, which is the only unknown left in the coupled-flow problem. The volume flow rate in the corner channels is

$$Q = \iint_{A} u \, dy \, dz, \tag{3.11}$$

where $A = A_T - \bar{A}$ is the cross-sectional area of the corner channels shown in figure 1(*c*), and is known since $A_T = 4B$ and $\bar{A}$ is listed in table 1. The sum of $\bar{Q}$ and Q gives the total flow rate through the microchannel.

4. Solution of coupled unidirectional flows

4.1. *Linear expansions*

The streamwise velocities u and $\bar{u}$ depend on four independent parameters: D, $\bar{P}_x$, λ and B. Since D and $\bar{P}_x$ appear linearly in (3.2) and (3.6), we can extract their dependence by the following linear expansions:

$$u = U_D D + U_P \bar{P}_x, \tag{4.1}$$

$$\bar{u} = \bar{U}_D D + \bar{U}_P \frac{\bar{P}_x}{\lambda}, \tag{4.2}$$

where the expansion coefficients U_D, U_P, $\bar{U}_D$, and $\bar{U}_P$ depend only on λ and B. Although D does not appear in (3.2), it does affect the drop flow through the coupling with the corner flow at the corner interfaces, and $\bar{U}_D$ reflects this induced flow.

Substitution of (4.1) and (4.2) into the governing equations (3.2) and (3.6), and the interfacial conditions (3.7) and (3.8) gives

$$\nabla^2 U_D = 1, \quad \nabla U_D \cdot n = \lambda \nabla \bar{U}_D \cdot n, \tag{4.3a,b}$$

$$\nabla^2 \bar{U}_D = 0, \quad \bar{U}_D = U_D, \tag{4.4a,b}$$

$$\nabla^2 U_P = 1, \quad \nabla U_P \cdot n = \nabla \bar{U}_P \cdot n, \tag{4.5a,b}$$

$$\nabla^2 \bar{U}_P = 1, \quad \bar{U}_P = \lambda U_P. \tag{4.6a,b}$$

The no-slip boundary condition at the wall in (3.9) yields

$$U_D = U_P = \bar{U}_D = \bar{U}_P = 0. \tag{4.7}$$

Along the symmetry planes shown in figure 2, $\bar{U}_D$ and $\bar{U}_P$ have zero normal gradient.

The above equations show that U_D and $\bar{U}_D$, and U_P and $\bar{U}_P$ are coupled through the boundary conditions at the corner interface. The coupled systems are solved by a finite-element method using the Matlab partial differential equation toolbox (Mathworks 2017), as described in § A.1. The numerical code is validated in several ways (§ A.2). Contours of the velocity coefficients U_D, U_P, $\bar{U}_D$ and $\bar{U}_P$ are shown in figure 3 for $\lambda = 0.1$, 1, and 10 in a square microchannel. A detailed explanation of the contours is provided in § A.3. The velocity coefficients are expanded in asymptotic series in the limit $\lambda \to 0$ in appendix B to reveal the effects of drop viscosity.

4.2. *Volume flow rates*

4.2.1. *Drop and corner volume flow rates*

The drop velocity $\bar{u}$ in (4.2) is substituted into (3.10) to yield the drop volume flow rate as

$$\bar{Q} = D\bar{Q}_D + \frac{\bar{P}_x}{\lambda}\bar{Q}_P = -\bar{A}Ca, \tag{4.8a}$$

where

$$\bar{Q}_D = \iint_{\bar{A}} \bar{U}_D \, \mathrm{d}y \, \mathrm{d}z, \quad \bar{Q}_P = \iint_{\bar{A}} \bar{U}_P \, \mathrm{d}y \, \mathrm{d}z, \tag{4.8b,c}$$

and $-\bar{A}Ca$ is the drop plug-flow rate, which is specified. Since $\bar{Q}_D$ and $\bar{Q}_P$ depend only on B and λ, this integral constraint determines the drop-fluid pressure gradient:

$$\bar{P}_x = \frac{\lambda}{\bar{Q}_P}(-\bar{A}Ca - D\bar{Q}_D). \tag{4.9}$$

The carrier-liquid velocity u in (4.1) is substituted into (3.11) to give the corner-flow volume flow rate as

$$Q = DQ_D + \bar{P}_x Q_P, \tag{4.10a}$$

where

$$Q_D = \iint_{A} U_D \, \mathrm{d}y \, \mathrm{d}z, \quad Q_P = \iint_{A} U_P \, \mathrm{d}y \, \mathrm{d}z. \tag{4.10b,c}$$

The coefficients $\bar{Q}_D$, $\bar{Q}_P$, Q_D and Q_P are calculated numerically as detailed in §§ A.1 and A.2; they depend on the aspect ratio B and the viscosity ratio λ, and are plotted in figure 4 and presented in table 2 for $B = 1$, 1.2, 1.5 and 2, with $\lambda = 0$–100. The coefficients are all negative, and their behaviour in figure 4 is discussed in § A.3. The coefficients are expanded in asymptotic series in the limit $\lambda \to 0$ in § B.3, and the first two terms of the series are also plotted in figure 4. They agree with the full solution for $0 \leqslant \lambda < 0.2$.

4.2.2. *Total volume flow rate in the microchannel*

The total volume flow rate in the drop-moving direction is
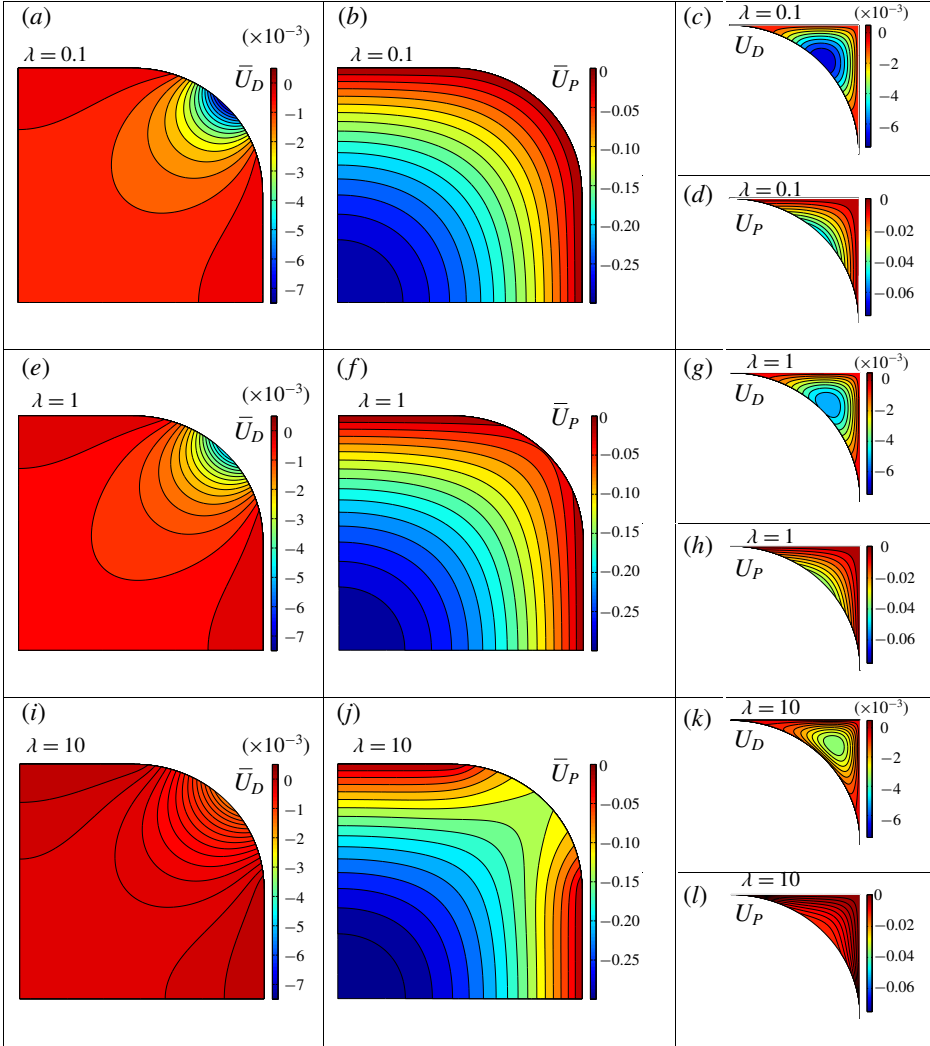
$$Q_T = -(\bar{Q} + Q). \tag{4.11}$$

FIGURE 3. (Colour online) Contours of the velocity expansion coefficients $\bar{U}_D$, $\bar{U}_P$, U_D, and U_P in a square microchannel for viscosity ratio $\lambda = 0.1$ (*a–d*), 1 (*e–h*) and 10 (*i–l*). The coefficients are defined in (4.1) and (4.2).

From (4.8a), the drop volume flow rate $\bar{Q} = -\bar{A}Ca$. The corner volume flow rate Q is also determined when $\bar{P}_x$ in (4.9) is substituted into (4.10). Thus, the total volume flow rate is found as

$$Q_T = \left(\frac{q_D}{LCa^{1/3}} + q_U \right) Ca, \qquad (4.12a)$$

where

$$q_D = \left(\lambda \frac{\bar{Q}_D Q_P}{\bar{Q}_P} - Q_D \right) \frac{C_D}{\bar{A}}, \quad q_U = \left(1 + \lambda \frac{Q_P}{\bar{Q}_P} \right) \bar{A}, \qquad (4.12b,c)$$

depend only on λ and B. If $\lambda = 0$, the solution reduces to that of an inviscid bubble obtained by Wong *et al.* (1995*b*) (see the validation discussion in § A.2).
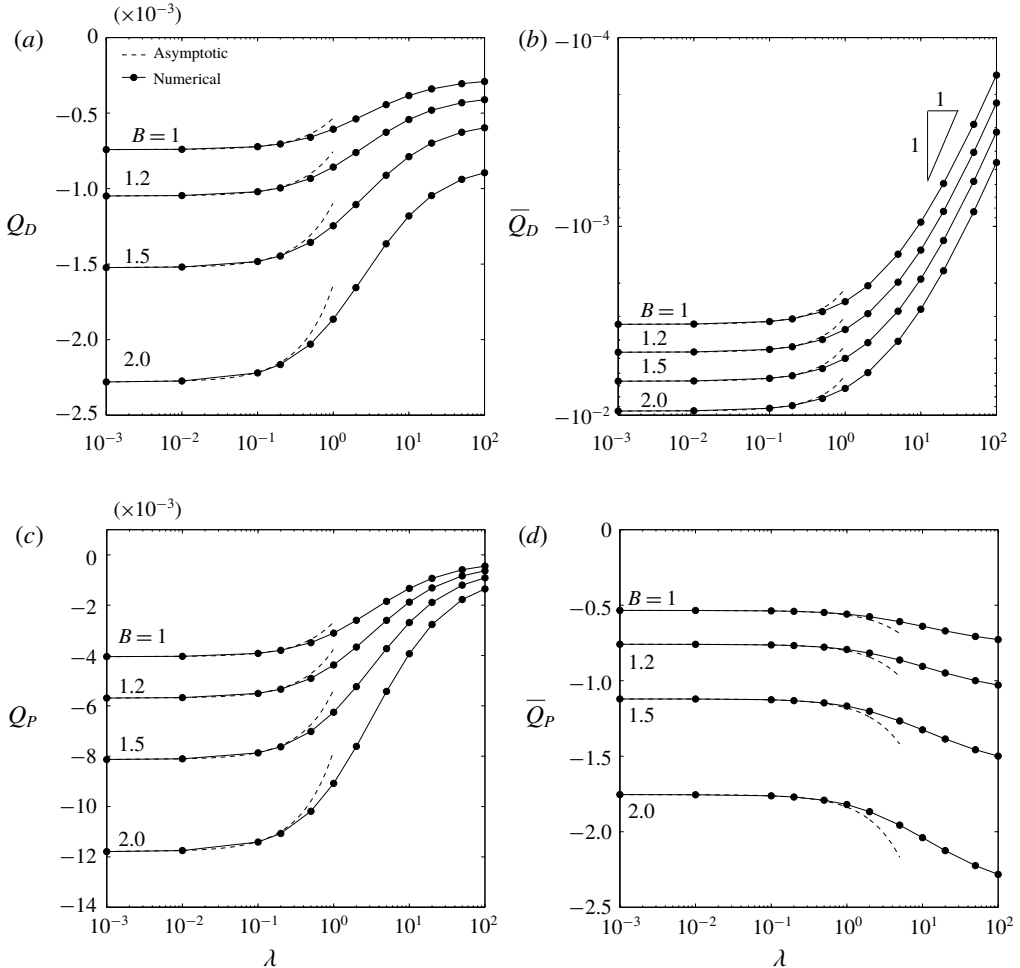
FIGURE 4. Volume-flow-rate coefficients Q_D (*a*), $\bar{Q}_D$ (*b*), Q_P (*c*), and $\bar{Q}_P$ (*d*), defined in (4.8) and (4.10), versus viscosity ratio λ for various aspect ratio B. The asymptotic solutions in the limit $\lambda \to 0$ in (B 13)–(B 16) are also plotted for comparison.

The coefficients q_D and q_U are listed in table 3 and plotted in figures 5(*a*) and 5(*b*), respectively, as a function of λ for various aspect ratio B. The coefficient q_D comes from a part of the corner flow driven by the contact-line-drag density D. We will call the q_D term the 'drag component' for the rest of this paper. The drag component represents a major portion of the corner flow, and is simply called the corner flow sometimes in this paper. For fixed B, q_D approaches a constant as $\lambda \to 0$, as shown in figure 5(*a*), because in this limit the drop becomes inviscid and the corner flow sees zero shear stress at the corner interface. As λ increases, the resistance to corner flow increases and q_D decreases. As $\lambda \to \infty$, the corner flow experiences no slip at the drop surface and q_D again becomes uniform. For fixed λ, the corner flow increases with B because of the larger flow area.

The coefficient q_U in (4.12*c*) consists of the drop plug flow (first term) and a minor portion of the corner flow (second term). The second term approaches zero as $\lambda \to 0$, and increases linearly with λ as $\lambda \to \infty$ because both Q_P and $\bar{Q}_P$ become constant

Aspect ratio	Coefficients ($\times 10^{-3}$)	Viscosity ratio, λ												
		0	0.001	0.01	0.1	0.2	0.5	1	2	5	10	20	50	100
$B = 1.0$	Q_D	-0.7422	-0.7420	-0.74401	-0.7224	-0.7046	-0.6604	-0.6068	-0.5386	-0.4440	-0.3840	-0.3402	-0.3052	-0.2912
	Q_P	-4.046	-4.044	-4.032	-3.914	-3.794	-3.491	-3.110	-2.602	-1.849	-1.334	-0.9332	-0.5935	-0.4491
	$\bar{Q}_D$	-3.303	-3.302	-3.292	-3.192	-3.090	-2.830	-2.503	-2.064	-1.405	-0.9496	-0.5930	-0.2882	-0.1580
	$\bar{Q}_P$	-534.8	-534.8	-535.1	-537.8	-540.6	-548.3	-559.2	-576.3	-609.1	-639.5	-670.6	-706.9	-728.0
$B = 1.2$	Q_D	-1.049	-1.049	-1.046	-1.021	-0.9958	-0.9334	-0.8576	-0.7612	-0.6275	-0.5427	-0.4808	-0.4314	-0.4115
	Q_P	-5.692	-5.690	-5.673	-5.507	-5.339	-4.911	-4.375	-3.662	-2.603	-1.878	-1.314	-0.8367	-0.6336
	$\bar{Q}_D$	-4.643	-4.641	-4.627	-4.486	-4.343	-3.978	-3.518	-2.901	-1.975	-1.335	-0.8336	-0.4053	-0.2221
	$\bar{Q}_P$	-758.9	-758.9	-759.3	-763.0	-767.0	-777.7	-793.0	-816.9	-862.8	-905.2	-948.8	-999.6	-1029
$B = 1.5$	Q_D	-1.523	-1.523	-1.519	-1.483	-1.446	-1.356	-1.246	-1.106	-0.9116	-0.7884	-0.6984	-0.6267	-0.5977
	Q_P	-8.133	-8.130	-8.105	-7.869	-7.628	-7.019	-6.254	-5.236	-3.725	-2.690	-1.887	-1.205	-0.9144
	$\bar{Q}_D$	-6.609	-6.607	-6.586	-6.386	-6.182	-5.663	-5.008	-4.130	-2.813	-1.902	-1.188	-0.5779	-0.3168
	$\bar{Q}_P$	-1121	-1121	-1121	-1126	-1132	-1147	-1168	-1202	-1266	-1325	-1386	-1457	-1499
$B = 2.0$	Q_D	-2.280	-2.280	-2.274	-2.220	-2.165	-2.030	-1.865	-1.656	-1.366	-1.181	-1.046	-0.9387	-0.8951
	Q_P	-11.79	-11.79	-11.75	-11.41	-11.07	-10.19	-9.080	-7.610	-5.426	-3.930	-2.766	-1.776	-1.355
	$\bar{Q}_D$	-9.514	-9.510	-9.480	-9.193	-8.900	-8.155	-7.215	-5.953	-4.060	-2.748	-1.719	-0.8374	-0.4595
	$\bar{Q}_P$	-1754	-1754	-1755	-1762	-1770	-1791	-1820	-1867	-1956	-2039	-2125	-2224	-2282

TABLE 2. Numerical solutions of the volume-flow-rate coefficients Q_D, Q_P, $\bar{Q}_D$ and $\bar{Q}_P$, defined in (4.10) and (4.8), for various viscosity ratio λ and microchannel aspect ratio B.

S. S. Rao and H. Wong

Aspect ratio	Coefficients	Viscosity ratio, λ												
		0	0.001	0.01	0.1	0.2	0.5	1	2	5	10	20	50	100
$B = 1.0$	q_D (×10^{-3})	2.636	2.635	2.628	2.557	2.487	2.313	2.106	1.847	1.501	1.293	1.150	1.041	0.9996
	q_U	3.759	3.759	3.759	3.762	3.764	3.771	3.780	3.793	3.816	3.837	3.864	3.917	3.991
	k_D	3.551	3.551	3.551	3.549	3.547	3.542	3.536	3.526	3.511	3.499	3.489	3.479	3.474
	k_U	0	0.007029	0.07025	0.6990	1.391	3.428	6.722	13.05	30.86	58.78	112.1	265.9	516.3
$B = 1.2$	q_D (×10^{-3})	3.468	3.468	3.457	3.365	3.272	3.044	2.771	2.431	1.976	1.703	1.513	1.370	1.315
	q_U	4.513	4.513	4.513	4.516	4.519	4.527	4.538	4.553	4.581	4.607	4.638	4.702	4.791
	k_D	3.306	3.306	3.306	3.304	3.302	3.298	3.291	3.283	3.268	3.257	3.248	3.239	3.235
	k_U	0	0.005947	0.05944	0.5915	1.177	2.902	5.691	11.05	26.15	49.86	95.13	225.7	438.6
$B = 1.5$	q_D (×10^{-3})	4.819	4.819	4.805	4.678	4.549	4.236	3.858	3.386	2.753	2.372	2.107	1.907	1.830
	q_U	5.654	5.654	5.654	5.658	5.662	5.671	5.684	5.703	5.737	5.769	5.808	5.888	5.999
	k_D	3.164	3.164	3.164	3.162	3.161	3.156	3.151	3.142	3.129	3.119	3.110	3.101	3.097
	k_U	0	0.005044	0.05044	0.5021	0.9989	2.465	4.841	9.408	22.33	42.67	81.59	194.0	377.2
$B = 2.0$	q_D (×10^{-3})	7.183	7.183	7.162	6.975	6.785	6.322	5.762	5.064	4.126	3.554	3.154	2.852	2.734
	q_U	7.577	7.577	7.578	7.582	7.586	7.599	7.615	7.639	7.682	7.723	7.774	7.880	8.027
	k_D	3.150	3.150	3.150	3.149	3.147	3.143	3.138	3.130	3.118	3.108	3.099	3.091	3.087
	k_U	0	0.004320	0.04317	0.4300	0.8562	2.115	4.163	8.117	19.37	37.16	71.31	170.3	332.0

TABLE 3. Coefficients q_D, q_U, k_D and k_U for various viscosity ratio λ and microchannel aspect ratio B. The coefficients q_D and q_U give the total volume flow rate Q_T in (4.12), whereas k_D and k_U give the carrier-liquid pressure gradient P_x in (4.16).
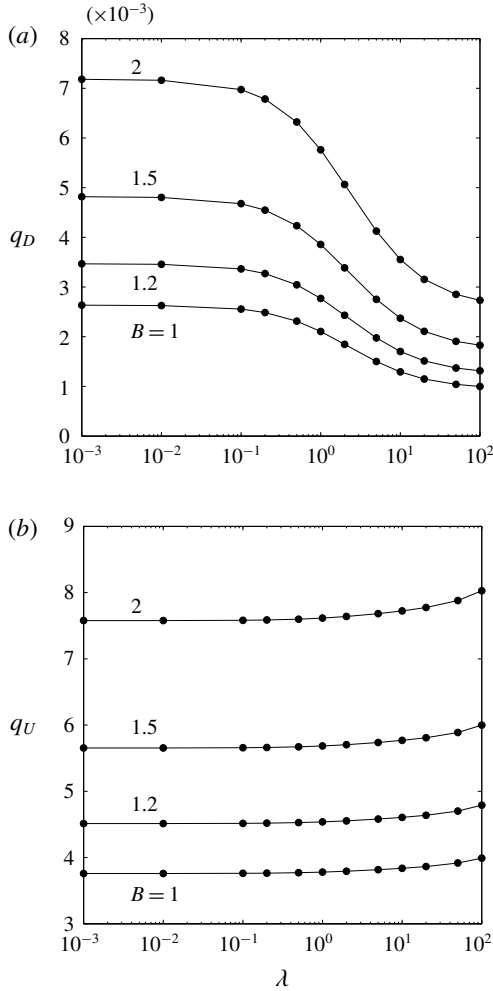
FIGURE 5. Coefficients q_D (a) and q_U (b) of the total volume flow rate defined in (4.12b,c) versus viscosity ratio λ for various aspect ratio B.

as $\lambda \to \infty$ (figures 4c and 4d). However, this increase in flow rate is small compared with the first term within the range of λ studied ($\lambda \leqslant 100$), as shown in figure 5(b), where $q_U = \bar{A}$ for $\lambda \ll 1$ and increases only slightly with λ for fixed B. Thus, we call the q_U term the 'plug component' for the rest of this paper.

Equation (4.12a) shows that the value of $LCa^{1/3}$ determines whether the drag or plug component dominates. For $LCa^{1/3} \to 0$, the drag component dominates and

$$Q_T \to \frac{q_D}{L} Ca^{2/3}. \tag{4.13}$$

Thus, for moderately long drops ($1 \ll L \ll Ca^{-1/3}$), the total flow rate varies nonlinearly with the drop velocity. The carrier liquid bypasses the drop through the corner channels, leading to a total volume flow rate that is much higher than that of the drop plug-flow rate ($\sim Ca$). For $LCa^{1/3} \gg 1$, the plug component dominates and

$$Q_T \to q_U Ca. \tag{4.14}$$

Thus, for extremely long drops ($L \gg Ca^{-1/3}$), the total flow rate varies linearly with the drop velocity. There is negligible corner flow and the drop moves as a leaky piston.

4.3. *Pressure gradients*

4.3.1. *Pressure gradient in the drop*

The pressure gradient in the drop in (4.9) can be written as

$$\bar{P}_x = \left(-\frac{\bar{k}_D}{LCa^{1/3}} + \bar{k}_U \right) Ca, \qquad (4.15a)$$

where

$$\bar{k}_D = \lambda \left(\frac{\bar{Q}_D}{\bar{Q}_P} \right) \frac{C_D}{\bar{A}}, \quad \bar{k}_U = -\frac{\lambda \bar{A}}{\bar{Q}_P} \qquad (4.15b,c)$$

are positive constants that depend only on B and λ. The coefficients $\bar{k}_D$ and $\bar{k}_U$ are plotted in figures 6(*a*) and 6(*b*), respectively, as a function of λ for $B = 1$, 1.2, 1.5 and 2. Since $\bar{k}_D$ is proportional to C_D, the first term in (4.15*a*) is the drag component. For fixed B, $\bar{k}_D$ follows the behaviour of $\lambda \bar{Q}_D$ because $\bar{Q}_P$ does not vary widely over $0 \leqslant \lambda \leqslant 100$, as shown in figure 4(*d*). Thus, $\bar{k}_D \sim \lambda$ as $\lambda \to 0$ and reaches a plateau as $\lambda \to \infty$. The drop flow $\bar{Q}_D$ is induced by the corner flow Q_D, which is driven by the contact-line-drag density D. The corner flow Q_D bypasses the drop and induces a drop flow ($\bar{Q}_D$) towards the front of the drop. Since the drop is closed, this induced flow will be stopped at the front end of the drop and raise the pressure there. Thus, the drag component of $\bar{P}_x$ in (4.15*a*) is negative.

The $\bar{k}_U$ term comes from the drop plug flow specified in (4.8*a*). Hence, this term is the plug component, which drives the drop fluid forwards and is positive. Figure 6(*b*) shows that $\bar{k}_U$ increases almost linearly with λ, because $\bar{Q}_P$ is insensitive to variation in λ (figure 4*d*).

4.3.2. *Pressure gradient in the carrier liquid*

The pressure gradient in the carrier liquid is found by substituting $\bar{P}_x$ in (4.15*a*) into the integral force balance (3.4):

$$P_x = \left(\frac{k_D}{LCa^{1/3}} + k_U \right) Ca, \qquad (4.16a)$$

where

$$k_D = \frac{C_D}{\bar{A}} - \bar{k}_D = \frac{C_D}{\bar{A}} \left(1 - \lambda \frac{\bar{Q}_D}{\bar{Q}_P} \right), \quad k_U = \bar{k}_U \qquad (4.16b,c)$$

are positive constants that depend only on B and λ. The coefficients k_D and k_U are listed in table 3, and k_D is plotted in figure 7 as a function of λ for $B = 1$, 1.2, 1.5 and 2 ($k_U = \bar{k}_U$, which is plotted in figure 6*b*). The k_D term in (4.16*a*) represents the pressure gradient required to overcome the contact-line-drag density D and is therefore the drag component. The coefficient k_D is positive since $\lambda \bar{Q}_D/\bar{Q}_P < 1$ always. As $\lambda \to 0$, $\lambda \bar{Q}_D/\bar{Q}_P \to 0$ because both $\bar{Q}_D$ and $\bar{Q}_P$ become constant, as shown in figures 4(*b*) and 4(*d*). As $\lambda \to \infty$, $\lambda \bar{Q}_D/\bar{Q}_P$ is finite because $\bar{Q}_D \sim 1/\lambda$ as $\lambda \to \infty$ (figure 4*b*). Furthermore, $\lambda \bar{Q}_D/\bar{Q}_P < 1$ in the limit $\lambda \to \infty$, so that $k_D > 0$ always.

The k_U term represents the pressure gradient that balances the film and corner drags on the drop and is the plug component. Since $k_U = \bar{k}_U$, both P_x and $\bar{P}_x$ have the same plug component.
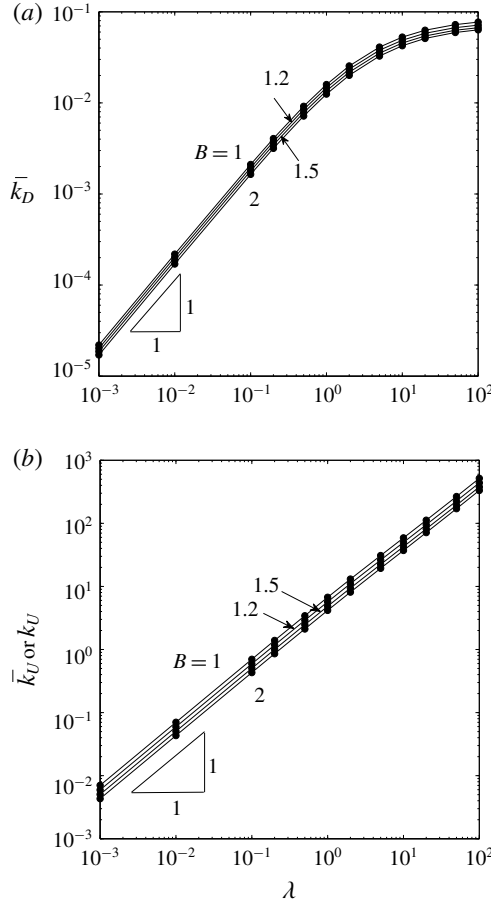
FIGURE 6. Coefficients $\bar{k}_D$ (*a*) and $\bar{k}_U$ (*b*) of the drop-fluid pressure gradient defined in (4.15*b,c*) versus viscosity ratio λ for various aspect ratio *B*. Coefficient k_U of the carrier-liquid pressure gradient defined in (4.16*a*) is the same as $\bar{k}_U$.

4.3.3. *Summary of pressure-gradient results*

To summarize the results for pressure gradients, when $LCa^{1/3} \ll 1$, the drag component (corner flow) dominates and

$$\bar{P}_x \sim P_x \sim \frac{Ca^{2/3}}{L}, \qquad (4.17)$$

although $\bar{P}_x$ is negative and P_x is positive. When $LCa^{1/3} \gg 1$, the plug component dominates and

$$\bar{P}_x = P_x \sim \lambda Ca. \qquad (4.18)$$

When $L = \bar{k}_D/(\bar{k}_U Ca^{1/3})$, $\bar{P}_x = 0$ because its two components cancel. When $\lambda = 0$, $\bar{k}_D = \bar{k}_U = k_U = 0$ and we recover the solution of Wong *et al.* (1995*b*) for long bubbles.
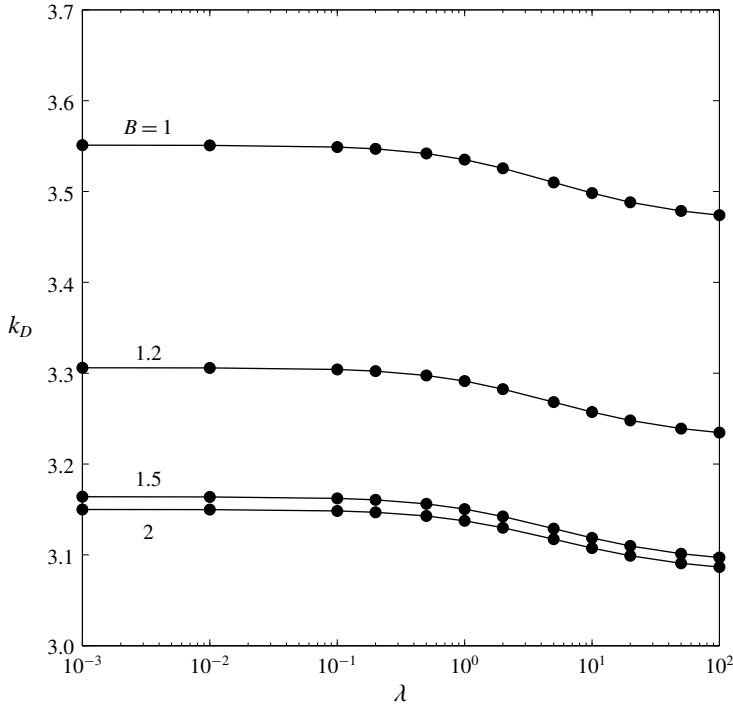
FIGURE 7. Coefficient k_D of the carrier-liquid pressure gradient defined in (4.16b) versus viscosity ratio λ for various aspect ratio B.

4.4. *Velocity fields*

Substituting $\bar{P}_x$ in (4.9) into (4.1) and (4.2) gives the velocity fields in the carrier liquid and drop as

$$u = \left[\left(U_D - \frac{\lambda \bar{Q}_D}{\bar{Q}_P} U_P \right) \frac{C_D/\bar{A}}{LCa^{1/3}} - \frac{\lambda \bar{A}}{\bar{Q}_P} U_P \right] Ca, \qquad (4.19)$$

$$\bar{u} = \left[\left(\bar{U}_D - \frac{\bar{Q}_D}{\bar{Q}_P} \bar{U}_P \right) \frac{C_D/\bar{A}}{LCa^{1/3}} - \frac{\bar{A}}{\bar{Q}_P} \bar{U}_P \right] Ca. \qquad (4.20)$$

Both u and $\bar{u}$ can be separated into a drag component, which dominates as $LCa^{1/3} \to 0$ (or $1 \ll L \ll Ca^{-1/3}$), and a plug component, which dominates as $LCa^{1/3} \to \infty$ (or $L \gg Ca^{-1/3}$). The drag component of u is dominated by U_D, because $\lambda \bar{Q}_D/\bar{Q}_P \ll 1$ for all λ and B studied, and $U_P \sim U_D$, as shown by Q_P and Q_D in figure 4. The plug component of u follows U_P, and has the same sign as U_P because $\bar{Q}_P$ is negative. Since both U_D and U_P are negative (figure 3), the drag and plug components of u are negative, i.e., the corner flow always moves in the same direction as the drop.

4.4.1. *The drag component of drop-fluid flow*

The drag component of $\bar{u}$ can be positive over part of the drop domain and, in these positive regions, the drop fluid is moving opposite to the direction of the drop.

To identify these positive flow regions, we define

$$\bar{u}_D = \bar{U}_D - \frac{\bar{Q}_D}{\bar{Q}_P} \bar{U}_P, \tag{4.21}$$

and plot it for a square microchannel in figure 8 for $\lambda = 0.1$ (*a*), 1 (*b*) and 10 (*c*). It shows that $\bar{u}_D$ is positive at the centre of the drop for all the λ values considered, and its magnitude decreases as λ increases. Thus, when the drag component (corner flow) dominates, the drop fluid is dragged by the corner flow from the back of the drop towards the front next to the corner interface, and moves from the front towards the back along the drop centre.

4.4.2. *The plug component of drop-fluid flow*

The plug component of $\bar{u}$ is always negative because $\bar{U}_P$ (figure 3) is everywhere negative and $\bar{Q}_P$ is obtained by integrating $\bar{U}_P$ over the drop area as defined in (4.8*c*). Thus, when the plug component dominates, the drop fluid flows in the direction of the drop at every point of the drop domain. It is instructive to view this drop flow in a reference frame moving with the drop. Thus, we define

$$\bar{u}_U = 1 - \frac{\bar{A}}{\bar{Q}_P} \bar{U}_P. \tag{4.22}$$

This shifted plug component is plotted for a square microchannel in figure 8 for $\lambda = 0.1$ (*d*), 1 (*e*) and 10 (*f*). The velocity contours show that for $\lambda \ll 1$, the drop fluid circulates in an almost axisymmetric roll, similar to a drop in a circular microchannel. For $\lambda \gg 1$, the drop fluid circulates in four planar rolls, one on each sidewall. This viscous-drop velocity profile has higher velocity gradients and therefore would allow better mixing of the drop fluid.

5. Practical applications

Our model assumes a drop moving at a dimensionless velocity Ca and obtains pressure gradients, flow rates and velocity fields that depend on Ca. In practice, usually a pressure difference is imposed between the two ends of a microchannel and the resulting flow rates measured. Thus, in this section, we apply our flow-field solutions to derive the pressure-gradient versus flow-rate relation (§ 5.1). Furthermore, we will also derive results that are of practical interest, such as the coefficient of mobility (§ 5.2), the excess pressure gradient (§ 5.3), the velocity ratio for two drops of unequal lengths (§ 5.4), and the pressure gradient for a train of drops (§ 5.5).

5.1. *Pressure-gradient versus flow-rate relation*

The primary objective of this work is to determine the relation between the total volume flow rate and the carrier-liquid pressure gradient needed to drive the steadily moving long drop. Dividing P_x in (4.16*a*) by Q_T in (4.12*a*) gives

$$P_x = H Q_T, \tag{5.1a}$$

where we define

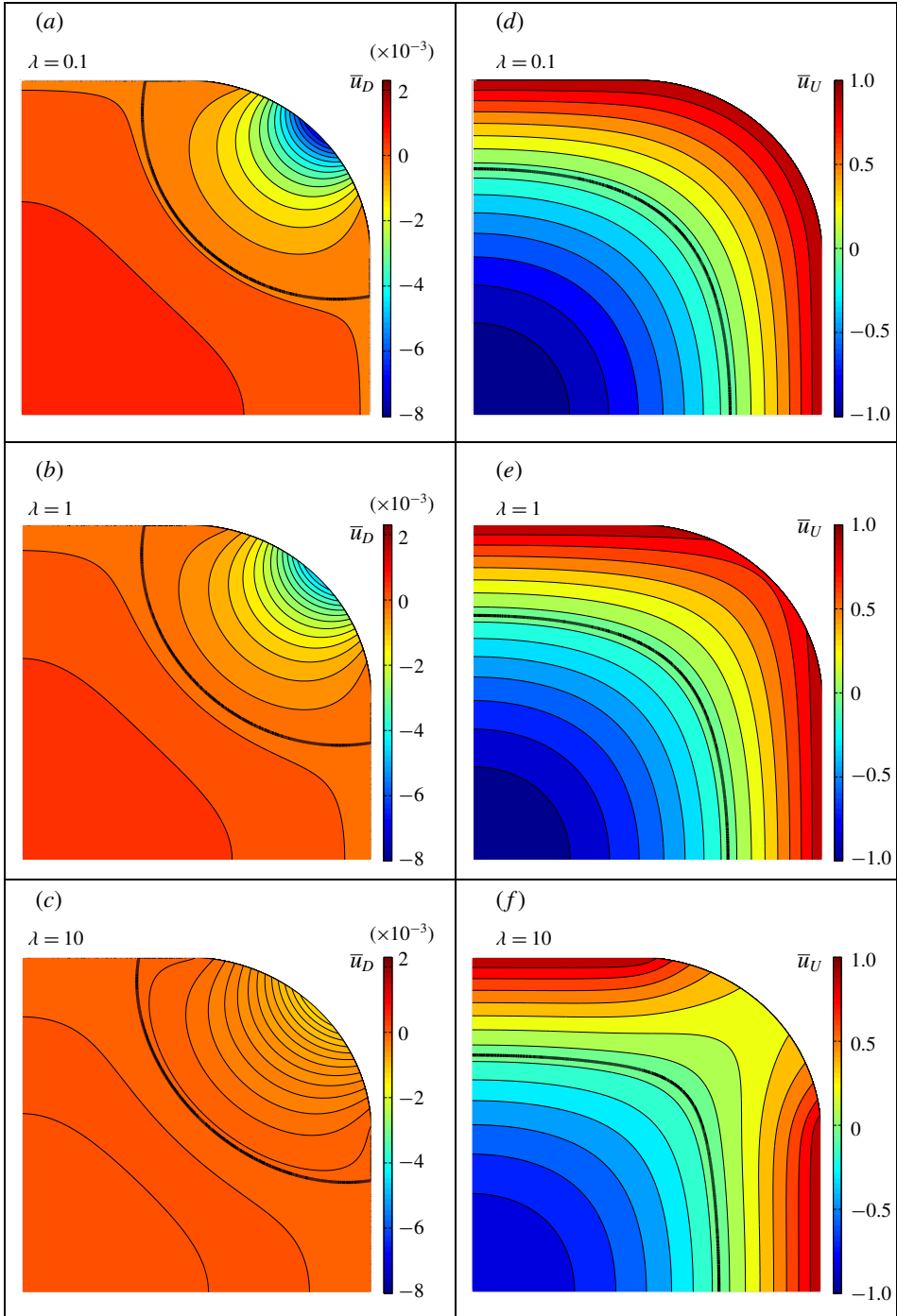$$H = \frac{k_D + k_U L C a^{1/3}}{q_D + q_U L C a^{1/3}} \tag{5.1b}$$

FIGURE 8. (Colour online) Velocity contours of the normalized drag component $\bar{u}_D$ (a–c) and the shifted plug component $\bar{u}_U$ (d–f) of the drop-fluid flow in a square microchannel for $\lambda = 0.1$ (a,d), $\lambda = 1$ (b,e), and $\lambda = 10$ (c,f). The velocity $\bar{u}_D$ is defined in (4.21), and $\bar{u}_U$ in (4.22). In each plot, the thick line indicates zero velocity, and the net volume flow is zero.

as the dimensionless hydraulic resistance for drop flow. When the drag component (corner flow) dominates, $LCa^{1/3} \to 0$ and

$$H \to \frac{k_D}{q_D} \equiv H_D. \tag{5.2}$$

When the plug component dominates, $LCa^{1/3} \to \infty$ and

$$H \to \frac{k_U}{q_U} \equiv H_U. \tag{5.3}$$

Thus, in both limits, H is constant and P_x varies linearly with Q_T. Note that in the limit $LCa^{1/3} \to 0$, both P_x and Q_T vary nonlinearly with drop speed ($P_x \sim Ca^{2/3}$ and $Q_T \sim Ca^{2/3}$). Away from the two limits, H varies with $LCa^{1/3}$, and P_x varies nonlinearly with Q_T because $Q_T = Q_T(Ca)$, as shown in (4.12a). In appendix C, we find $P_x = P_x(Q_T)$ by eliminating Ca in H.

The hydraulic resistances H_D and H_U are plotted as a function of λ for various B in figures 9(a) and 9(b), respectively. It shows that H_D increases with λ for fixed B, despite that both k_D and q_D decrease as λ increases (figures 7 and 5a). Figure 9(b) shows that $H_U \sim \lambda$ for fixed B. Thus, the drop viscosity has much stronger effect on the plug flow than on the corner flow. In figure 10, H is plotted as a function of $LCa^{1/3}$ for $\lambda = 0$ and 100 and $B = 1$ and 2. It shows that H decreases as $LCa^{1/3}$ increases. Thus, the hydraulic resistance is highest when the drag component (or corner flow) dominates.

5.2. *Coefficient of mobility*

The ratio of drop velocity to average velocity of the channel flow is commonly known as the coefficient of mobility and is usually measured in drop-flow experiments (Jakiela *et al.* 2011):

$$\beta = \frac{Ca\,A_T}{Q_T} = \frac{4B}{\dfrac{q_D}{L\,Ca^{1/3}} + q_U}. \tag{5.4}$$

In figure 11, β is plotted as a function of $LCa^{1/3}$ for viscosity ratio $\lambda = 0$ and 100, and aspect ratio $B = 1$ and 2. It shows that for constant $LCa^{1/3}$ and B, β increases with λ if $LCa^{1/3} \ll 1$, and β decreases as λ increases if $LCa^{1/3} \gg 1$. This is because q_D and q_U in (4.12b,c) vary differently with λ, as shown in figure 5. Thus, when the drag component (corner flow) dominates, more viscous drops are more mobile; when the plug component (plug flow) dominates, less viscous drops are more mobile. For fixed λ and $LCa^{1/3}$, β decreases as B increases for all $LCa^{1/3}$. This is because the corner-flow area increases with B, leading to a higher corner flow that reduces β.

5.3. *Excess pressure gradient*

We have determined the pressure gradient P_x required to drive a long drop surrounded by a carrier liquid through a rectangular microchannel at the volume flow rate Q_T. The carrier liquid in the microchannel far away from the drop is also moving with the volume flow rate Q_T and is driven by a dimensionless pressure gradient P_{xs}:
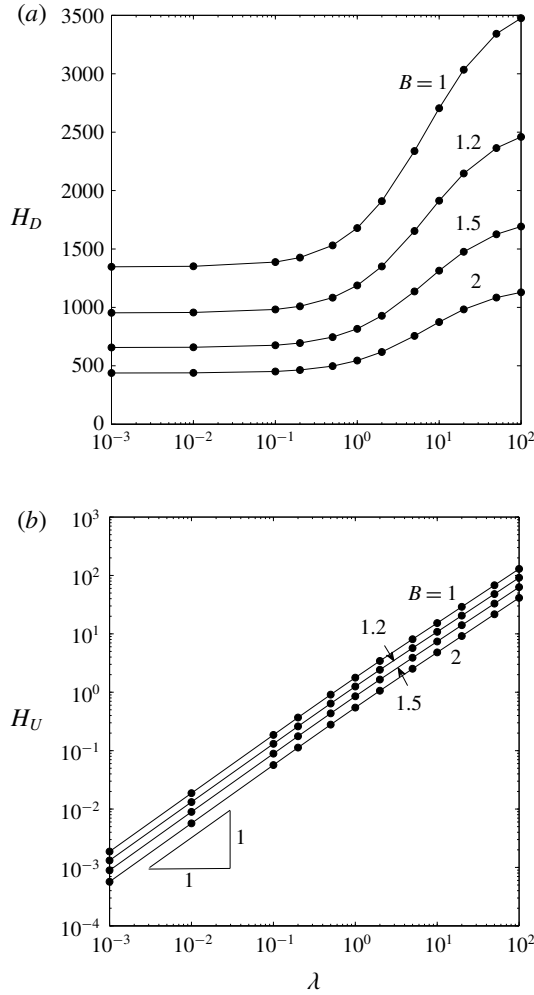
$$P_{xs} = k_s Q_T \tag{5.5a}$$

FIGURE 9. Dimensionless hydraulic resistance H_D (*a*) and H_U (*b*) defined, respectively, in (5.2) and (5.3) versus viscosity ratio λ for various aspect ratio B.

$$k_s = \frac{3}{4B}\left[1 - \frac{192}{\pi^5 B}\sum_{n=1,3,5,\dots}^{\infty}\frac{\tanh(n\pi B/2)}{n^5}\right]^{-1}, \tag{5.5b}$$

where k_s is the dimensionless hydraulic resistance for a single-phase fluid flowing unidirectionally in a rectangular duct of aspect ratio B (White 1991). Values of k_s are presented in table 1. Thus, we define an excess pressure gradient as

$$\Delta P_x = P_x - P_{xs} = \left[\frac{e_D}{LCa^{1/3}} + e_U\right]Ca, \tag{5.6a}$$
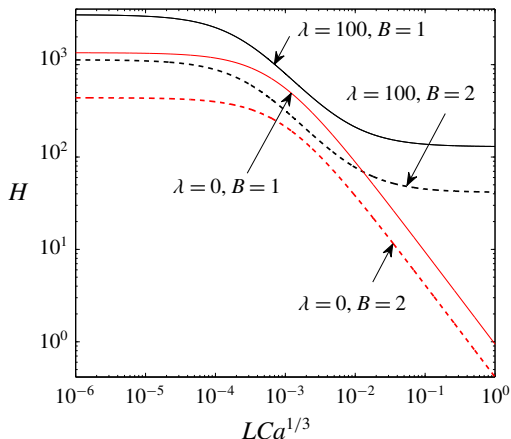
where

$$e_D = k_D - k_s q_D, \tag{5.6b}$$

FIGURE 10. (Colour online) Dimensionless hydraulic resistance H defined in (5.1) of drop flow versus $LCa^{1/3}$ for $\lambda = 0$ and 100, and $B = 1$ and 2.
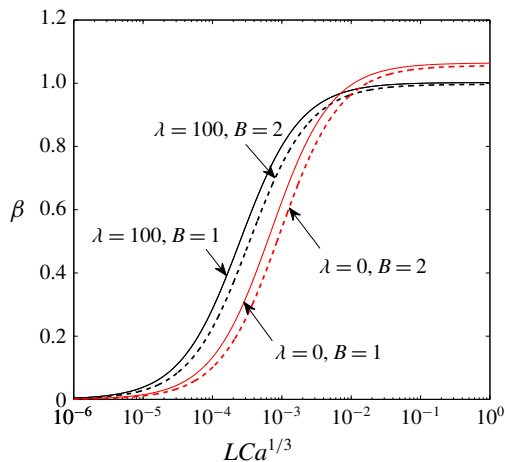

FIGURE 11. (Colour online) Mobility β defined in (5.4) versus $LCa^{1/3}$ for $\lambda = 0$ and 100, and $B = 1$ and 2.

$$e_U = k_U - k_s q_U. \tag{5.6c}$$

The coefficient e_D follows k_D because $k_s q_D < 1.4 \times 10^{-3} k_D$ for all λ and B studied (see figures 5a and 7). Thus, e_D is always positive. This means that when the drag component (corner flow) dominates, the drop-flow pressure gradient always exceeds the single-phase carrier-liquid pressure gradient, assuming that both are moving at the same volume flow rate. This is because the carrier liquid must move at a higher speed in bypassing the drop through the narrow corner channels. The higher liquid speed and the narrower flow area lead to a higher pressure gradient, resulting in a positive excess pressure gradient. The coefficient e_U is plotted in figure 12 as a function of λ for various B. It shows that e_U is positive for $\lambda > 1$ and negative for $\lambda < 1$, independent of B. Thus, the excess pressure gradient is negative when the plug flow dominates and $\lambda < 1$. This is because when the plug flow dominates, the resistance to drop
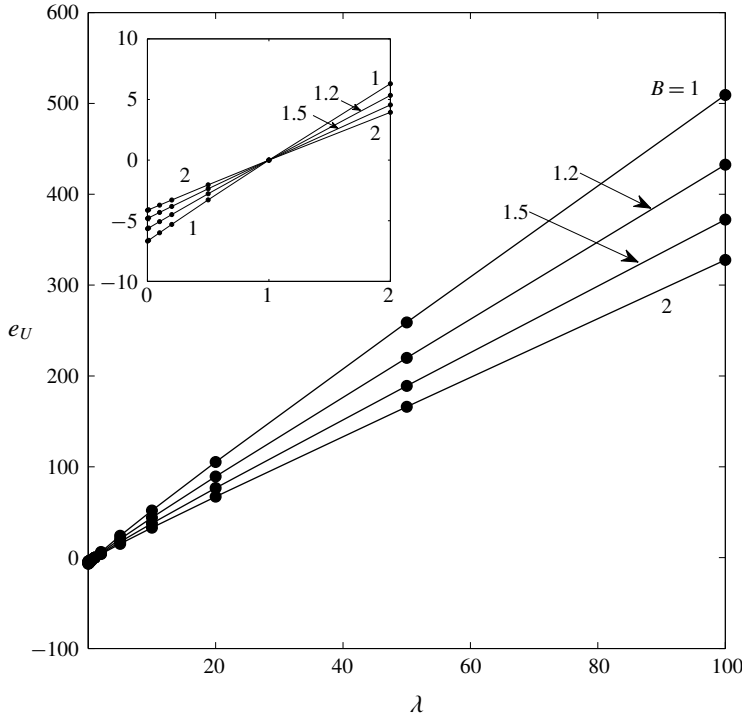
FIGURE 12. Coefficient e_U of the excess pressure gradient defined in (5.6c) versus viscosity ratio λ for various aspect ratio B.

motion comes from the shear forces on the drop. If $\lambda < 1$, then the drop is less viscous compared with the carrier liquid, and the shear forces on the drop will also be comparatively smaller. Thus, the drop can be driven by a smaller pressure gradient and the excess pressure gradient is negative. The result of $e_U = 0$ at $\lambda = 1$ further confirms the accuracy of k_U and q_U.

5.4. *Velocity ratio for two drops of unequal lengths*

Consider two long drops of lengths L_1 and L_2 ($>L_1$) moving in a rectangular microchannel at velocities U_1 and U_2, respectively. The two drops contain the same fluid and are sufficiently far apart that they do not influence each other. We study the velocity ratio U_2/U_1 when both drops are driven by either (i) the same channel volume flow rate or (ii) the same channel pressure gradient.

5.4.1. *Constant channel volume flow rate*

If both drops are flowing in the same channel one after another, then the channel volume flow rate Q_T is the same, and (4.12a) gives

$$\left(\frac{q_D}{L_1 Ca_1^{1/3}} + q_U \right) U_1 = \left(\frac{q_D}{L_2 Ca_2^{1/3}} + q_U \right) U_2, \tag{5.7}$$
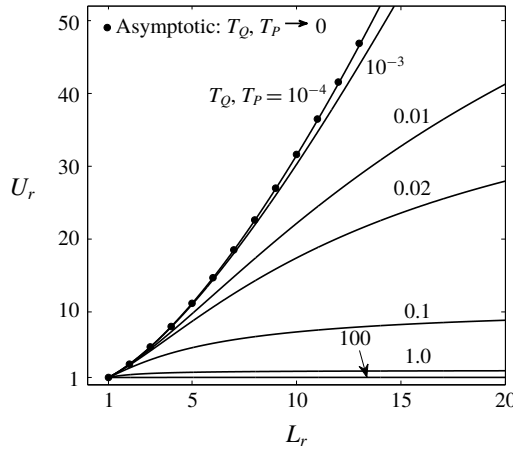
FIGURE 13. Drop-velocity ratio versus drop-length ratio for various T_Q (or T_P) defined in (5.8*a*) (or (5.12*a*)). The asymptotic solution is listed in (5.9).

where $Ca_1 = \mu U_1 / \sigma$, $Ca_2 = \mu U_2 / \sigma$, and q_D and q_U are the same for both drops (figure 5). The above equation can be written as

$$U_r = 1 + \frac{L_r U_r^{1/3} - 1}{T_Q L_r U_r^{1/3} + 1}, \qquad (5.8a)$$

where

$$U_r = \frac{U_2}{U_1}, \quad L_r = \frac{L_2}{L_1}, \quad T_Q = \frac{q_U}{q_D} L_1 Ca_1^{1/3}. \qquad (5.8b-d)$$

Here, T_Q is a positive dimensionless parameter that depends only on the first drop. When the corner flow dominates, $L_1 Ca_1^{1/3} \to 0$, so that $T_Q \to 0$, and (5.8*a*) yields

$$U_r \to L_r^{3/2}. \qquad (5.9)$$

Thus, the velocity ratio increases nonlinearly with the length ratio. When the plug flow dominates, $L_1 Ca_1^{1/3} \to \infty$ and therefore $T_Q \to \infty$, so that (5.8*a*) reduces to

$$U_r \to 1. \qquad (5.10)$$

The asymptotic relations in (5.9) and (5.10) are independent of B and λ.

In figure 13, U_r is plotted against L_r for various T_Q. It shows that for a given L_r, U_r decreases as T_Q increases or as the plug flow becomes dominant. For fixed T_Q, U_r increases with L_r, and according to (5.8*a*), as $L_r \to \infty$, $U_r \to 1 + 1/T_Q$. Thus, when the first-drop length and speed are fixed, the second drop moves faster as its length increases. This is because a longer drop has reduced corner flow, which leads to a higher drop speed so as to maintain a constant total volume flow rate. As $L_r \to \infty$, the corner flow ceases completely, leading to a constant speed for the second drop.

5.4.2. *Constant channel pressure gradient*

If two identical microchannels are arranged in parallel, and each contains a drop, then the pressure gradient P_x is the same in both systems, and (4.16a) gives

$$\left[\frac{k_U}{L_1 Ca_1^{1/3}} + k_D\right] U_1 = \left[\frac{k_U}{L_2 Ca_2^{1/3}} + k_D\right] U_2, \qquad (5.11)$$

where k_U and k_D are the same for both drops (figures 6b and 7). The above equation can be written as

$$U_r = 1 + \frac{L_r U_r^{1/3} - 1}{T_P L_r U_r^{1/3} + 1}, \quad T_P = \frac{k_U}{k_D} L_1 Ca_1^{1/3}, \qquad (5.12a,b)$$

where T_P is a positive dimensionless parameter that relies solely on the first drop. Since (5.12a) is the same as (5.8a), the results in §5.4.1 also hold here when T_Q is replaced by T_P (figure 13).

In summary, if a drop of length L_1 in a microchannel is followed by another drop of length L_2 ($> L_1$), the longer drop will move faster and catch up with the first drop if the drag component (corner flow) dominates. Further, if the two drops merge, the resulting drop, which is even longer, will move faster than the original drops. For a train of drops in a microchannel, the drops will have a higher tendency to coalesce because of the possible non-uniformity in drop length if the drag component (corner flow) dominates. If the plug component dominates, the drops will stay separated.

5.5. *Train of drops*

5.5.1. *Pressure gradient*

Consider a steady train of uniform drops of dimensionless length L with uniform dimensionless spacing L_S between them. If the spacing $L_s (\gg 1)$ is large compared to the channel width, then the carrier liquid flows mainly unidirectionally between drops and obeys (5.5a): $P_{xs} = k_s Q_T$. The dimensionless pressure gradient in the carrier liquid across a drop is given in (5.1a): $P_x = HQ_T$. Thus, the dimensionless pressure gradient across a unit cell of the drop train is

$$P_{xT} = \frac{L}{L_T} P_x + \frac{L_S}{L_T} P_{xs} = H_T Q_T, \qquad (5.13)$$

$$H_T = \alpha H + (1 - \alpha) k_s, \qquad (5.14)$$

where $L_T = L + L_S$ is the total length of the unit cell, $\alpha = L/L_T$ is the dispersed phase length fraction, and H_T is the dimensionless hydraulic resistance of the drop train. Hence, the pressure-gradient versus flow-rate relation for various drop-train systems may be analysed. The length fraction α is the only additional parameter needed to define a drop-train system compared with a single-drop system.

5.5.2. *Continuous injection of drop fluid and carrier liquid*

A drop train is usually generated by injecting the carrier liquid and the drop fluid continuously from separate fluid reservoirs at the inlet of the test section. If the carrier-liquid injection flow rate Q_{iC}^* and the drop-fluid injection flow rate Q_{iD}^* are made dimensionless to give $Q_{iC} = Q_{iC}^* \mu/\sigma W^2$ and $Q_{iD} = Q_{iD}^* \mu/\sigma W^2$, then their sum is equal to the dimensionless total flow rate:

$$Q_{iC} + Q_{iD} = Q_T. \qquad (5.15)$$

The total flow rate is also equal to the sum of corner flow and drop flows, i.e., $Q_T = |Q| + |\bar{Q}|$, according to (4.11). However, $|Q| \neq Q_{iC}$ and $|\bar{Q}| \neq Q_{iD}$ in general. To derive their relations, we consider a control volume that encloses the injection ports and the test section. Although the drop fluid enters the control volume continuously, it exits discretely, and the usual mass-balance equation cannot be applied. Instead, a discrete time interval Δt must be considered during which a unit cell of the drop train leaves the control volume:

$$\Delta t = \frac{L_T}{Ca}, \tag{5.16}$$

where Δt has been non-dimensionalized by $\mu W/\sigma$. Then, the mass of the control volume will remain constant at successive times separated by Δt. Thus, over an interval Δt, the volume of drop fluid entering the control volume must equal the volume of a single drop:

$$Q_{iD}\Delta t = L\bar{A} \tag{5.17a}$$

or

$$Q_{iD} = \frac{L\bar{A}Ca}{L_T} = \alpha|\bar{Q}|. \tag{5.17b}$$

Consequently,

$$Q_{iC} = |Q| + (1 - \alpha)|\bar{Q}|. \tag{5.18}$$

Thus, once Q_{iC}, Q_{iD}, and α are specified, we can find $|\bar{Q}|$ and $|Q|$. Since $Ca = |\bar{Q}|/\bar{A}$, and L, B and λ are known for a particular drop-train system, the pressure gradient for the drop train can be calculated using (5.13). The mobility in (5.4) can also be computed. Thus, the drop-train system is completely characterized.

6. Comparison with experiments

Several experimental studies on drop flow in rectangular microchannels have been published. Since these studies emphasized different aspects of drop flow, the results were presented using different parameters. We will convert their parameters into the ones defined in this paper for comparison.

6.1. *Comparison with Kim et al. (2014)*

6.1.1. *Parameter conversion*

Kim *et al.* (2014) studied the motion of deionized water drops in perfluorocarbon containing 10 % (v/v) of a nonionic fluoro-soluble surfactant in rectangular microchannels machined in polycarbonate. The drop to carrier-liquid viscosity ratio $\lambda = 0.534$, as determined from their table 2. The channel walls were treated to improve wettability by the carrier liquid. We compare with the experiments performed on the ER4 chip described in their paper because the data presented are the most complete. The rectangular test channel for the ER4 chip has half-width $W = 92.3$ µm and $B = 1.05$, as shown in their table 1. The carrier and drop liquids are injected continuously at the inlet of the system. For each set of experiments, the carrier-liquid flow rate Q_{iC}^* is held constant, and different drop liquid flow rate Q_{iD}^* is set. Based on these flow rates, the authors defined two superficial velocities:

$$J_C^* = \frac{Q_{iC}^*}{A_T^*}, \quad J_D^* = \frac{Q_{iD}^*}{A_T^*}, \tag{6.1a,b}$$

and a carrier-liquid volumetric flow ratio:

$$\beta_C = \frac{Q_{iC}^*}{Q_{iC}^* + Q_{iD}^*} = \frac{J_C^*}{J_C^* + J_D^*}. \tag{6.2}$$

The dimensionless drop length $L/2B$ and drop spacing $L_s/2B$ are then plotted as a function of β_C for various J_C^* in their figures 7(*a*) and 7(*b*), respectively. Since the capillary number is not presented in their paper, we find it by the following method. For each data point in figure 7(*a*) in their paper, we get $L/2B$, β_C and J_C^*. We then calculate J_D^* from (6.2) and subsequently $Q_{iD} = Q_{iD}^*\mu/\sigma W^2 = J_D^* A_T^* \mu/\sigma W^2$ with A_T^*, μ and σ values listed in their table 2. From their figure 7(*b*), we get $L_s/2B$ for the corresponding values of β_C and J_C^* in their figure 7(*a*). Thus, we obtain the dispersed phase length fraction $\alpha = L/(L + L_s)$. Hence, we can find $Ca = Q_{iD}/\alpha\bar{A}$ from (5.17*b*) with $\bar{A} = 3.948$ for $B = 1.05$ as calculated by interpolating between the values listed in table 1. Thus, we have all the five parameters (B, λ, L, Ca, α) needed to completely characterize a drop-train system.

6.1.2. *Comparison of mobility*

From the definition of mobility in (5.4),

$$\beta = \frac{Ca\,A_T}{Q_T} = \frac{\sigma\,Ca}{\mu(J_C^* + J_D^*)}. \tag{6.3}$$

This determines the experimental value of β. Our model in (5.4) gives $\beta = \beta(LCa^{1/3})$ with $q_D = 2.486 \times 10^{-3}$ and $q_U = 3.961$ for $B = 1.05$ and $\lambda = 0.534$. The comparison is presented in table 4. We limit the comparison for drop trains with $L > 5$ as our model holds only for long drops, and drops with $L > 5$ have a well-defined middle section. The comparison shows that $\beta(\text{model}) = 1.06$ for all the cases considered and $\beta(\text{exp}) < \beta(\text{model})$. The comparison improves for longer drops, in general. The experimental value of $LCa^{1/3}$ suggests that the plug flow dominates, resulting in $\beta \approx 1$.

6.1.3. *Comparison of pressure gradient*

The pressure difference across the test section was measured by differential pressure transducers (Kim *et al.* 2014). The pressure difference divided by the channel length gives the pressure gradient. Since the channel is filled by a train of drops with uniform length and spacing, the pressure gradient in the channel is the same as that over a unit cell of the drop train. Kim *et al.* (2014) reported in their figure 9(*b*) the ratio of this pressure gradient (P_{xT} in (5.13)) to the single-phase pressure gradient based on the carrier-liquid volume flow rate, $P_{xC} = k_s Q_{iC}$, as a function of β_C. In our model, this pressure-gradient ratio is

$$\frac{P_{xT}}{P_{xC}} = \frac{H_T Q_T}{k_s Q_{iC}} = \left[\frac{\alpha H}{k_s} + (1 - \alpha)\right]\frac{Q_T}{Q_T - \alpha|\bar{Q}|}, \tag{6.4}$$

where H_T in (5.14) and Q_{iC} in (5.18) have been substituted. The drop-flow rate $|\bar{Q}| = \bar{A}Ca$ according to (4.8*a*), the total volume flow rate $Q_T = Q_T(B, \lambda, L, Ca)$ as shown in (4.12*a*), the hydraulics resistance $H = H(B, \lambda, LCa^{1/3})$ following (5.1*b*), and the single-phase dimensionless hydraulic resistance $k_s = k_s(B)$ based on (5.5*b*). For the experiments, $B = 1.05$ and $\lambda = 0.534$. Hence, the experimental values of L, α, and Ca in table 4A are sufficient to evaluate the pressure-gradient ratio.

| Experiment | From figures 7(a) and 7(b) of Kim et al. (2014) | | | | | | | | |
	J_C^* (×10⁻³ m s⁻¹)	$L/2B$	$L_S/2B$	β_c	L (expt.)	α (expt.)	J_D^* (×10⁻³ m s⁻¹)	Q_{ID} (×10⁻³)	Ca (expt.) (×10⁻³)
Kim (a) 1	2.3	14.4	0.994	0.112	30.1	0.935	18.2	10.1	2.73
2		10.6	1.15	0.144	22.2	0.902	13.7	7.59	2.13
3		9.74	1.15	0.168	20.4	0.894	11.4	6.33	1.79
4		8.63	1.23	0.201	18.1	0.875	9.17	5.08	1.47
5		5.96	1.59	0.251	12.5	0.790	6.87	3.81	1.22
6		4.61	1.83	0.358	9.68	0.716	4.12	2.28	0.808
7		3.34	2.50	0.501	7.01	0.571	2.29	1.27	0.564
Kim (b) 1	4.7	6.16	0.477	0.201	12.9	0.928	18.9	10.5	2.85
2		2.98	0.517	0.251	6.26	0.852	14.1	7.83	2.33
3		2.82	0.437	0.286	5.92	0.866	11.8	6.54	1.91
4		2.70	2.15	0.527	5.67	0.557	4.24	2.35	1.07
Kim (c) 1	7.0	8.51	1.19	0.201	17.9	0.877	27.9	15.5	4.47
2		3.30	0.676	0.274	6.93	0.830	18.6	10.3	3.14
Kim (d) 1	9.3	3.82	0.875	0.286	8.01	0.814	23.2	12.9	4.00
2		3.34	0.915	0.308	7.01	0.785	20.9	11.6	3.74
3		3.18	0.954	0.334	6.68	0.769	18.5	10.3	3.38
4		2.90	0.994	0.363	6.09	0.745	16.3	9.04	3.07
5		2.70	1.07	0.401	5.67	0.716	13.9	7.70	2.72
6		2.43	1.15	0.445	5.09	0.678	11.6	6.43	2.40

TABLE 4A. Data from Kim et al. (2014) performed on the ER4 chip described in their figures 7(a) and 7(b). These data allow L, α and Ca to be calculated as described in § 6.1.1.

Experiment		$LCa^{1/3}$ (expt.)	H	β (expt.) (6.3)	β (model) (5.4)	% Error	$\dfrac{P_{xT}}{P_{xC}}$ (expt.)	$\dfrac{P_{xT}}{P_{xC}}$ (model) (6.4)	% Error
Kim (a)	1	4.21	1.086	1.01	1.06	4.98	12.9	10.2	20.9
	2	2.86	1.184	1.01	1.06	4.93	9.07	7.47	17.7
	3	2.48	1.230	0.990	1.06	7.05	7.54	7.21	4.46
	4	2.06	1.303	0.971	1.06	9.04	8.90	6.47	27.3
	5	1.34	1.532	1.01	1.06	4.99	7.84	4.49	42.8
	6	0.902	1.848	0.953	1.06	11.1	5.22	3.84	26.3
	7	0.579	2.388	0.929	1.06	13.9	4.78	2.95	38.2
Kim (b)	1	1.83	1.356	0.916	1.06	15.7	8.08	11.3	−39.7
	2	0.827	1.935	0.934	1.06	13.3	9.90	7.71	22.1
	3	0.734	2.070	0.876	1.06	20.8	9.25	9.01	2.64
	4	0.580	2.389	0.902	1.06	17.3	4.87	2.84	41.7
Kim (c)	1	2.94	1.175	0.969	1.06	9.31	7.05	6.03	14.4
	2	1.01	1.740	0.930	1.06	13.8	7.62	6.14	19.5
Kim (d)	1	1.27	1.566	0.933	1.06	13.5	5.98	5.14	14.0
	2	1.09	1.682	0.938	1.06	13.0	5.98	4.73	20.8
	3	1.00	1.751	0.920	1.06	15.1	6.03	4.55	24.6
	4	0.886	1.866	0.909	1.06	16.5	5.69	4.32	24.1
	5	0.793	1.982	0.890	1.06	19.0	5.27	4.04	23.2
	6	0.682	2.161	0.870	1.06	21.6	4.60	3.78	17.8

TABLE 4B. Predicted mobility and pressure-gradient ratio compared with the experimental values presented in figure 9(b) of Kim et al. (2014). In the experiments, $B = 1.05$, and $\lambda = 0.534$. The predicted mobility (pressure-gradient ratio) is consistently higher (lower) than the experimental values by an average of 13 (22) %. There is only one experiment (Kim(b) 1) in which the predicted pressure-gradient ratio is higher than the experimental value.

A comparison of the pressure-gradient ratio is shown in table 4B. The model predicted values increase with α, the same as in the experiments, and are lower on average by 22.4 %, except in one experiment (Kim (b)1). One possible explanation is the presence of surfactants in the experiments. If a drop moves as a plug, the surfactant at the thin-film interface is swept from the front towards the back end. Thus, the surface tension is higher at the front and lower at the back. The resulting Marangoni stress will oppose the motion of the drop and a higher pressure gradient is required to drive the drop at the same velocity, leading to the smaller mobilities shown in table 4. Mobility reduction by surfactants has been observed for bubble flow in rectangular microchannels (Fuerstman *et al.* 2007).

6.2. *Comparison with Vanapalli et al. (2009)*

Vanapalli *et al.* (2009) studied the hydrodynamic resistance of a single moving drop in a rectangular microchannel fabricated in polydimethylsiloxane (PDMS). The carrier liquid is mineral oil and the drop consists of a mixture of water and glycerol, the ratio of which is varied to achieve different viscosities. After their drop length and capillary number are converted to ours, their experiments yield $LCa^{1/3} = 0.780$–10.2, suggesting that the plug flow dominates. In their figure 7, the drop velocity is plotted against the mean velocity for $\lambda = 0.03$ and 0.88 and various L, and the slope gives the mobility as $\beta = 1.28$. This value is higher than our predicted value shown in figure 11. Also, their mobility is independent of drop length, viscosity ratio and capillary number for the range of parameters studied, similar to our model prediction in figure 11. They compared the pressure difference across a single drop with that across the single-phase carrier liquid by a microfluidic comparator. Their figure 6B shows that the pressure difference decreases with increase in drop viscosity, whereas our model predicts that the pressure difference increases with drop viscosity. Furthermore, their excess pressure difference is positive for $\lambda \ll 1$, whereas our model predicts that the excess pressure difference should be negative for $\lambda \ll 1$ and positive for $\lambda > 1$ when the plug flow dominates. The reason for the disagreement is not clear.

6.3. *Comparison with Jakiela et al. (2011, 2012)*

6.3.1. *Jakiela et al. (2011)*

Jakiela *et al.* (2011) measured the mobility of individual water droplets in hexadecane in a square microchannel micro-milled in polycarbonate. The channel walls were treated with dodecylamine to guarantee complete wetting by hexadecane. Great care was taken to ensure that the system is free of surfactant. The viscosity ratio was varied in the range $\lambda = 0.3$–33 by adding glycerine to water, and the drop length was varied from $L = 2$ to 56. The carrier-liquid pressure difference across the system is varied to generate $Ca = 1.5 \times 10^{-4}$–1.1×10^{-1}. The experimental data for $\lambda = 0.3$ and 1 show that when $LCa^{1/3} \approx 1$ or higher, the mobility $\beta \approx 1$, in agreement with our model (figure 11). For $\lambda = 3$ and 33.2, the mobility is found to decrease significantly with increasing $LCa^{1/3}$. Thus, longer drops lead to higher corner flow, resulting in lower mobility, which is opposite to our model predictions. Jin *et al.* (2012) measured the curvature of the end caps of long drops moving with $Ca = 0.003$ in a rectangular microchannel with $\lambda = 0.3$. They found that as L increases from 7 to 23, the radius of curvature at the tip of the front end stays constant, but that of the back end increases by approximately 20 %. It is clear from their figure 8 that the apparent contact angle at the back end increases with L, and that for $L = 23$, the angle $\approx 45°$. These increases can result from moving contact lines at the back end

(Davis 1980; Shikhmurzaev 1997), which will increase the contact-line drag at the back end significantly (Wong *et al.* 1995*b*). Our model assumes that the deposited film is intact, the viscosity ratio $\lambda \ll Ca^{-1/3}$ when $LCa^{1/3} \sim 1$ or $\gg 1$, and the moving drop deviates infinitesimally from the static drop shape (§ 7). These conditions seem to be violated for long viscous drops in Jakiela *et al.* (2011), and thus the results are not comparable.

6.3.2. *Jakiela et al. (2012)*

Jakiela *et al.* (2012) presented the velocity field inside a moving long drop for the same system studied in Jakiela *et al.* (2011). Their figure 4 shows two velocity fields for $Ca = 5 \times 10^{-4}$ and 2×10^{-3}, respectively, and $L \approx 5$, $\lambda = 0.33$ (private communication). The carrier liquid flows through the corner channels in both cases. However, the drop with $Ca = 5 \times 10^{-4}$ exhibits streamwise drop-fluid motion adjacent to the corner interface induced by the corner flow, whereas the drop with $Ca = 2 \times 10^{-3}$ does not. The observation of corner-induced drop flow when Ca is low is in general agreement with our model predictions. Our model reveals that when the drag component dominates, there is fast corner-induced fluid motion inside the drop (figure 8*a*). This corner-induced motion is absent when the plug component dominates (figure 8*d*). The drag component dominates when $LCa^{1/3} \ll 1$. However, the presence of moving contact lines will increase the contact-line drag significantly and may enhance the drag component at higher $LCa^{1/3}$. The corner-induced drop flow has also been observed by Kinoshita *et al.* (2007).

The difficulty in characterizing drop flow in microchannels is reflected by the scatter in the experimental mobility data as described by Jakiela *et al.* (2011). We hope that this work provides an improved analytical understanding of the physics of drop motion.

7. Discussion

7.1. *Velocity scales and limits on viscosity ratio λ*

A long drop in a rectangular microchannel is driven by the carrier liquid, which can either push the drop (plug flow) or bypass the drop through the corner channels (corner flow). These two flows have different velocity scales. When the plug flow dominates, both the drop-fluid and carrier-liquid velocities scale with the drop velocity as

$$\delta \bar{u}^* \sim \delta u^* \sim U, \tag{7.1}$$

according to (4.19) and (4.20). These scales hold for $LCa^{1/3} \sim 1$ and $\gg 1$. When the corner flow dominates, $LCa^{1/3} \to 0$, and (4.19) and (4.20) give the velocity scales as

$$\delta \bar{u}^* \sim \delta u^* \sim \frac{U}{LCa^{1/3}}. \tag{7.2}$$

The shear stress in the thin film at the contact-line region is $\mu \partial u^*/\partial y^* \sim \mu U/Ca^{2/3}W$, because the no-slip condition at the wall gives $\delta u^* \sim U$ at the contact-line region even when the corner flow dominates and because the film thickness $\sim Ca^{2/3}W$. The contact-line region occupies an axial distance $\sim Ca^{1/3}W$ (Hodges *et al.* 2004). This axial length scale is transmitted to the drop fluid and establishes a small region in the drop fluid scaled by $\delta y^* \sim Ca^{1/3}W$ (Hodges *et al.* 2004). Thus, the shear stress exerted by the drop fluid on the interface at the contact-line region is $\bar{\mu} \partial \bar{u}^*/\partial y^* \sim$

$\bar{\mu}\delta\bar{u}^*/\delta y^* \sim \bar{\mu}\delta\bar{u}^*/(Ca^{1/3}W)$. This interfacial shear stress is negligible compared with the film shear stress if

$$\lambda \ll Ca^{-1/3}, \tag{7.3}$$

when the plug flow dominates or if

$$\lambda \ll L, \tag{7.4}$$

when the corner flow dominates. (Since $LCa^{1/3} \ll 1$ when the corner flow dominates, $L \ll Ca^{-1/3}$, so that the second upper bound is much smaller than the first one.) When these conditions are satisfied, the contact-line drag for bubbles derived by Wong *et al.* (1995*b*) can be applied for drops.

7.2. *Thin-film profiles*

Under conditions (7.3) and (7.4), the thin-film profiles derived for long bubbles by Wong *et al.* (1995*a*) also hold for long drops, because again the interfacial shear stress is negligible. Thin films are deposited by the front end of a long moving bubble (figure 1*a*). The microchannel wall drags liquid away from the front cap because of no slip. The liquid pressure ahead of the cap is lower than that in the relatively planar thin film, owing to capillarity, and this pressure gradient sucks liquid from the film back to the cap. A balance between these two forces determines the film thickness (Wong *et al.* 1995*a*). Since the contact line is curved (figure 1*a*), the drag force normal to the contact line decreases from the front to zero at the side, but the capillary-pressure gradient stays about the same normal to the contact line everywhere along the contact line. Consequently, the deposited film thickness decreases from $O(Ca^{2/3})$ at the front to $O(Ca)$ at the side. This film profile is frozen in a downstream distance $x \ll Ca^{-1}$. For $x \sim Ca^{-1}$, the film at the centre rearranges into a parabolic shape whereas the film at the side thins to $O(Ca^{4/3})$. The deposited non-uniform film profile and subsequent evolution have been observed in experiments (Chen, Li & Li 2016). The same film profiles should also hold for long drops if conditions (7.3) and (7.4) are satisfied.

The thin films deposited by a long drop may disintegrate if the drop is very long. At the side of the film, the film thickness is $O(Ca)$. For $Ca = 10^{-3}$ and $W = 100$ μm, the film can be as thin as $O(100$ nm$)$. Given the roughness of the channel walls (see, for example, figure S1 in Jakiela *et al.* 2012), it is likely that the deposited film will disintegrate before reaching the back end (Wong, Fatt & Radke 1996). Thus, the drop will be in direct contact with the wall, and the moving contact lines at the back end will increase the contact-line drag significantly (Wong *et al.* 1995*b*; Thompson & Troian 1997; Snoeijer & Andreotti 2013). Hence, the drag component (corner flow) will be important at higher $LCa^{1/3}$ than the predicted range in our model. This will lead to lower mobility and higher corner flow at higher $LCa^{1/3}$, as observed in experiments. Hence, it is critical to monitor the stability of deposited thin films, which unfortunately has not been performed in published drop-flow experiments. Since the thinnest film thickness $\sim Ca$ in rectangular microchannels (as opposed to $O(Ca^{2/3})$ in circular microchannels), it would be difficult to numerically simulate drop or bubble flow in rectangular microchannels, as resolving the thin-film regions is computationally expensive.

7.3. *Assumptions of our model*

The assumptions made in developing our model are summarized below. Our model holds in the limit the capillary number $Ca \to 0$. As Ca decreases, the thin films deposited by a long drop become thinner because their thickness varies from $O(Ca^{2/3})$ at the film centre to $O(Ca)$ at the film side. For extremely small capillary numbers, disjoining pressure can become important (Chaudhury, Acharya & Chakraborty 2014; Hammoud *et al.* 2017). Further, wall roughness can be significant for microchannels (for example, if they are machined in polycarbonate or etched in PDMS) and can cause the thin film to break. In this work, we assume that the film is intact and is sufficiently thick so that disjoining pressure plays no role. In using the solution of contact-line drag derived by Wong *et al.* (1995*b*) for long bubbles, we assume that $\lambda \ll Ca^{-1/3}$ when the plug flow dominates, and $\lambda \ll L$ when the corner flow dominates. Further, we assume that the corners of the microchannel are sharp, and the interface is clean. The length of the drop needs to be long ($L \gg 1$). However, the contact-line drag used in this paper holds for $L \ll Ca^{-1}$, i.e. the deposited film does not rearrange.

Another assumption of our model is that the shape of the moving drop deviates insignificantly from that of the static drop. This allows the static drop cross-sectional areas to be used in the fluid-flow calculations. When the corner flow dominates ($LCa^{1/3} \ll 1$), both the drop fluid and the carrier liquid are moving at $O[1/(LCa^{1/3})]$ times faster than the drop, as shown by (7.1) and (7.2). This fast corner flow is driven by a positive pressure gradient, whereas the induced drop flow establishes a negative pressure gradient, as indicated by (4.16*a*) and (4.15*a*). Thus, the carrier-liquid pressure decreases from the back end of the drop towards the front, whereas the drop-fluid pressure increases from the back towards the front. Consequently, the pressure jump across the interface increases along the drop. Will this pressure-jump increase over the length of the drop be sufficient to alter the curvatures of the end caps significantly? To answer this question, we examine (2.10). By rearranging the terms, we get

$$(\bar{p}_b - p_b) - (\bar{p}_f - p_f) = -\frac{C_D}{\bar{A}} Ca^{2/3}. \tag{7.5}$$

Thus, the pressure jump across the interface varies by $O(Ca^{2/3})$ over the length of the drop, which is much smaller than $(\bar{p}_b - p_b)$ or $(\bar{p}_f - p_f)$ because each is of $O(1)$.

7.4. *Speculations on surfactant effects*

Although the long moving drop is assumed free of surfactant in this work, the calculated velocity fields can predict qualitatively the effects of surfactant. For simplicity, we will consider a trace amount of an insoluble surfactant. When the plug flow dominates (figure 8*d*–*f*), there is negligible corner flow and the surfactant is swept from the front of the drop towards the back along the thin-film interfaces. The surfactant-concentration gradient will generate a surface-tension gradient, which can immobilize the film interface and lead to a higher film drag on the drop. The surface-tension difference between the two ends of the drop will drive a corner flow in the direction of the moving drop, because the corner channel area is $O(1)$ and is much larger than the film cross-section area ($\sim Ca^{2/3}$). This corner flow will reduce the streamwise surfactant-concentration gradient, and lead to a cross-stream surfactant-concentration gradient between the film and corner interfaces. The enhanced film drag will make the drop less mobile.

When the corner flow dominates (figure 8*a*–*c*), the surfactant is swept from the back of the drop towards the front along the corner interfaces. Since the drop is moving

much slower than the corner flow, the deposited thin films will remove negligible amount of surfactant. Thus, the surfactant will accumulate at the front cap and be depleted at the back cap. The resulting surface-tension gradient will immobilize the corner interfaces and reduce the corner flow. This will increase the mobility of the drop.

7.5. *Comparison between drop and bubble flows*

It is instructive to compare the results for long drops with those for long bubbles. The total volume flow rate Q_T in (4.12*a*) has two components, the same as in the bubble flow, and the coefficients q_D and q_U do not vary significantly from the bubble case of $\lambda = 0$ (figure 5). However, the pressure gradient of drop flow is different from that of bubble flow. The pressure gradient P_x in (4.16*a*) also has two components. The drag-component coefficient k_D is insensitive to λ (figure 7), but the plug component vanishes for $\lambda = 0$ and increases almost linearly with λ (figure 6*b*). Hence, the plug component is absent in bubble flow, but plays a significant role in drop flow when $\lambda L Ca^{1/3} \sim 1$ or $\gg 1$.

8. Conclusions

A long drop moving steadily in a rectangular microchannel filled otherwise with a carrier liquid is driven by the pressure gradient in the carrier liquid. The carrier-liquid pressure force $P_x L \bar{A}$ on the drop balances the film drag, the corner drag and the contact-line drag. The film and corner drags are found to equal to the drop-fluid pressure force $\bar{P}_x L A$ across the drop. Furthermore, the previously derived contact-line drag D_C in (2.8) for long bubbles can be applied to long drops if the viscosity ratio $\lambda \ll Ca^{-1/3}$ and $\lambda \ll L$. Hence, the carrier-liquid pressure gradient is given in (3.4) as

$$P_x = \bar{P}_x + D, \tag{8.1}$$

where $D = D_C / \bar{A} L$ is the contact-line-drag density. The pressure gradients also drive unidirectional flows inside and outside the long drop. After P_x is eliminated using (8.1), the coupled flows depend linearly on $\bar{P}_x$ and D. Hence, the fluid velocities are expanded as linear functions of $\bar{P}_x$ and D. The velocity expansion coefficients are solved using a finite-element method, and they depend on the viscosity ratio λ and aspect ratio B. The drop-fluid velocity is integrated across the drop cross-sectional area to yield the drop plug-flow rate, which is specified. This determines $\bar{P}_x$. Substitution into (8.1) yields P_x, which after converting back to dimensional form becomes

$$P_x^* = \left(\frac{k_D}{LCa^{1/3}} + k_U \right) \frac{\mu U}{W}, \tag{8.2}$$

and

$$Q_T^* = \left(\frac{q_D}{LCa^{1/3}} + q_U \right) W^2 U, \tag{8.3}$$

where Q_T^* is the dimensional total volume flow rate through the microchannel, and k_D, k_U, q_D and q_U are dimensionless constants that depend only on the viscosity ratio λ and the channel aspect ratio B, and are listed in table 3 and plotted in figures 5–7. The results show that if $LCa^{1/3} \ll 1$, then the contact-line drag dominates and the drop is retarded significantly so that the carrier liquid bypasses the drop through the corner channels. This corner flow drags the drop fluid forwards next to the corner

interface at a speed that is much faster than drop. This forward moving drop fluid returns along the drop centre towards the back end to satisfy the constant volume-flow-rate condition. If $LCa^{1/3} \gg 1$, then the contact-line drag is negligible, and the corner flow is basically stationary; the drop then moves as a leaky piston. We have obtained solutions for rectangular microchannels with $B = 1$, 1.2, 1.5 and 2, and fluid systems with $\lambda = 0$ to 100. We apply our model to study the motion of a train of long drops, and compare our model predictions with published experiments with mixed results.

Acknowledgements

Appendix A. Coupled streamwise flows

A.1. *Numerical methods*

The coupled system of equations (4.3)–(4.6) is solved by a finite-element method (FEM) using the Matlab partial differential equation (PDE) toolbox (Mathworks 2017). First, the flow-domain shapes are specified (figure 2). Then, a mesh is laid on each domain using the mesh generating and refining capabilities of the toolbox. For better accuracy and to prevent ill-conditioning, the meshing algorithm tries to generate equilateral triangular elements. Thus, even near the contact-line region, we obtain reasonably shaped triangles. The drop-fluid and carrier-liquid domains are meshed separately. However, the mesh is controlled so as to have common nodes (vertices) at the interface by initiating the mesh generation from the interface. This simplifies the sharing of velocities and velocity gradients between the two fluids at the interface. After a mesh is generated, the weak form of the governing equation is discretized with piecewise-linear basis functions to yield a linear system, which is inverted by a Matlab solver. The method is second-order accurate. Details of the mesh generation, discretization, and solution process have been documented for the Matlab PDE toolbox (Mathworks 2017).

The system of equations (4.3)–(4.6) can be separated into two sets of coupled equations: (4.3) and (4.4) for U_D and $\bar{U}_D$, and (4.5) and (4.6) for U_P and $\bar{U}_P$. The coupled system (4.3) and (4.4) is solved numerically in the following iterative sequence. The corner flow U_D governed by (4.3a) is first solved by imposing zero-stress boundary condition at the interface. The drop velocity $\bar{U}_D$ is then found from (4.4) with the calculated U_D values at the interface. The corner flow U_D is computed again from (4.3) with the newly calculated gradient of $\bar{U}_D$ at the interface. The iterative process continues until the velocity values in both domains converge to 8 significant digits. The same iterative procedure is used to solve the coupled system (4.5) and (4.6). We use an under-relaxation method to improve numerical stability during the iteration process for higher values of viscosity ratio λ.

The iterative procedure allows full utilization of the toolbox functions. The toolbox can impose either the Dirichlet or the Neumann boundary condition. Thus, each step in the iteration can simply utilize the standard toolbox function to arrive at a solution. The only modification is in calculating the normal gradient at the interface in the drop

in (4.3*b*) or (4.5*b*). This is achieved by fitting a second-order bi-polynomial to the drop velocities at a boundary node and four nearest nodes. This gives five equations. The sixth equation is obtained by requiring the bi-polynomial to satisfy the governing equation (4.4*a*) for $\bar{U}_D$ or (4.6*a*) for $\bar{U}_P$. Thus, we determine the six coefficients of the bi-polynomial. The velocity gradient at the boundary node is found by taking the derivative of the bi-polynomial in the direction normal to the interface. Once the normal velocity gradients are known in (4.3*b*) and (4.5*b*), the Neumann boundary condition in the toolbox can be directly implemented. The second-order bi-polynomial yields a second-order accurate solution for the velocity gradients, which matches the order of accuracy of FEM (Rao 2015).

The volume-flow-rate coefficients $\bar{Q}_D$, $\bar{Q}_P$, Q_D, and Q_P defined in (4.8) and (4.10) are computed as follows. For each coefficient, the velocity is integrated over the corresponding cross-sectional domain area, which has been discretized into triangular elements. Since the velocity has been solved by FEM, its values are known at the three nodes of each triangular element. The three node values are averaged and multiplied by the area of that element to give the elemental volume flow rate. (This is the 2D equivalent of the trapezoidal rule, and is second-order accurate.) Summing the elemental volume flow rates of all the elements in a unit cell and then multiplying the sum by four yields the volume-flow-rate coefficient. The coefficient is found to an accuracy of four significant digits, as verified by mesh refinement (Rao 2015). Similar numerical schemes have been used in solving coupled vapour and liquid unidirectional flows in polygonal micro heat pipes (Rao & Wong 2015).

A.2. *Validation of the numerical methods*

The computer programs are checked by verifying Green's theorem, which states that the area integral of the Laplacian of velocity over a flow domain is equal to the line integral of the normal velocity gradient around that domain boundary. The area integral agrees with the line integral to four significant digits for U_D, $\bar{U}_D$, U_P and $\bar{U}_P$ for all λ and B studied. This not only validates the numerical scheme for solving the velocity coefficients, but also confirms the correctness of the numerical integration procedure. The numerical results are also validated for the cases $\lambda = 1$ and 0. When $\lambda = 1$, the governing equations and boundary conditions for U_P and $\bar{U}_P$ in (4.5) and (4.6) reduce to those for a single-phase flow in a rectangular channel for which an analytic solution is available (White 1991). Comparing with the analytic solution, we find that the numerical solutions for the maximum velocity and the total volume flow rate $(Q_P + \bar{Q}_P)$ are accurate to four significant digits for all B cases studied. When $\lambda = 0$, the drop becomes a bubble, and our calculated carrier-liquid flow rate Q_D in the corners is compared with the values listed by Wong *et al.* (1995*b*), where they cited the results computed by Ransohoff & Radke (1988). Our solution agrees to one significant digit for $B = 1$ and to two significant digits for $B = 1.2, 1.5,$ and 2. However, the results computed by Ransohoff & Radke (1988) are not accurate because of the coarser grid used at that time, as pointed out by Patzek & Kristensen (2001), who presented more accurate data. Our Q_D values agree with Patzek & Kristensen (2001) to three significant digits for $B = 1$ and to four significant digits for $B = 1.2, 1.5,$ and 2. Patzek & Kristensen (2001) used approximately 3000 triangular elements in the corner domain, whereas we use 170 000 elements. Thus, our solutions listed in table 2 are accurate to at least four significant digits (Rao 2015).

A.3. *Explanation of results*

The coupled system (4.3) and (4.4) governs the corner flow U_D and the drop flow $\bar{U}_D$. The corner flow U_D is driven by a unit source in (4.3a) and the resulting shear stress and velocity at the interface drives $\bar{U}_D$, according to (4.3b) and (4.4). The interfacial boundary conditions show that the velocities are continuous at the interface, but the normal velocity gradients differ by a factor λ. When $\lambda = 0.1$, the corner flow U_D senses minimal shear stresses from the drop, as indicated by (4.3b), and the velocity contours are almost normal to the corner interface (figure 3c). As λ increases, U_D decreases as it is driven by the same unit source, but suffers higher shear resistance at the corner interface (figure 3g). At $\lambda = 10$, the drop is so viscous that it behaves like solid, and the corner flow sees almost no slip at the drop surface (figure 3k). The induced drop flow $\bar{U}_D$ decreases its magnitude as λ increases (figure 3a,e,i). This is because the driving shear stress at the interface decreases as $1/\lambda$ following (4.3b), resulting in smaller induced velocities.

Integrating U_D and $\bar{U}_D$ over their corresponding flow areas yields Q_D and $\bar{Q}_D$, respectively, as defined in (4.10b) and (4.8b). Thus, Q_D and $\bar{Q}_D$ in figure 4 can also be explained. As $\lambda \to 0$, the drop becomes inviscid and the corner flow Q_D sees zero shear resistance at the interface according to (4.3b). Thus, Q_D approaches a constant, as shown in figure 4(a). The induced drop flow $\bar{Q}_D$ is driven by the interfacial velocity following (4.4b) and also approaches a constant (figure 4b). As λ increases, both $|Q_D|$ and $|\bar{Q}_D|$ decrease because of the increasing shear resistance at the interface. As $\lambda \to \infty$, the drop behaves like solid and the corner flow Q_D sees no slip at the interface. Thus, Q_D again approaches a constant, as indicated in figure 4(a). The induced corner flow $\bar{Q}_D$ is driven by the velocity gradient at the interface, which varies as $1/\lambda$, as prescribed by (4.3b). Thus, $\bar{Q}_D \sim 1/\lambda$ as $\lambda \to \infty$, as shown in figure 4(b).

The second coupled system (4.5) and (4.6) governs the corner flow U_P and the drop flow $\bar{U}_P$. Both flows are driven by a unit source, and are coupled through the shear-stress balance and the kinematic condition at the interface. The shear-stress balance yields the same normal velocity gradients at the interface, whereas the kinematic condition states that the velocities at the interface differ by a factor λ. When $\lambda = 0.1$, $\bar{U}_P \approx 0$ at the corner interface according to (4.6b) because $U_P \sim 1$ based on (4.5a). Thus, $\bar{U}_P$ seems to obey the no-slip condition at the corner interface, as shown in figure 3(b). The figure also reveals that the streamwise shear stress is almost uniform at the corner interface, as indicated by the uniformly spaced velocity contours adjacent to the interface. This uniform shear stress is then imposed on the corner flow following (4.5b), resulting in the uniformly spaced velocity contours near the corner interface in figure 3(d). When $\lambda = 1$, the governing equations and boundary conditions in (4.5) and (4.6) can be combined, and the interface disappears to yield a single fluid. When $\lambda = 10$, the corner flow U_P is much weaker than the drop flow $\bar{U}_P$ based on (i) the kinematic boundary condition (4.6b) at the corner interface, and (ii) the corner channel area is much smaller than the drop area (Poiseuille flow depends sensitively on flow area). Thus, the corner flow velocity gradient is also much weaker. Consequently, the velocity contours of $\bar{U}_P$ in figure 3(j) are almost normal to the corner surface.

The corner flow Q_P and the drop flow $\bar{Q}_P$ are found by integrating U_P and $\bar{U}_P$, respectively, according to (4.10c) and (4.8c). Thus, their behaviour in figure 4 can also be explained. As $\lambda \to 0$, the drop flow $\bar{Q}_P$ sees zero velocity at the interface, as given by (4.6b). Thus, $\bar{Q}_P$ approaches a constant, and so does Q_P, as shown in figures 4(c) and 4(d). As λ increases, $|\bar{Q}_P|$ increases because it is allowed higher

velocity at the interface following (4.6*b*). Conversely, $|Q_P|$ decreases because its velocity at the interface must decrease. As $\lambda \to \infty$, both $\bar{Q}_P$ and Q_P will reach another plateau. As shown in figure 4, all coefficients increase their magnitudes as B increases for a fixed λ, because the drop and corner-flow areas increase with B.

Appendix B. Asymptotic expansions of the velocity coefficients in the limit $\lambda \to 0$

B.1. *Governing equations*

We expand the velocity coefficients in (4.1) and (4.2) as asymptotic series in λ:

$$U_D = U_1 + \lambda U_2 + \cdots , \tag{B 1}$$
$$U_P = V_1 + \lambda V_2 + \cdots , \tag{B 2}$$
$$\bar{U}_D = \bar{U}_1 + \lambda \bar{U}_2 + \cdots , \tag{B 3}$$
$$\bar{U}_P = \bar{V}_1 + \lambda \bar{V}_2 + \cdots . \tag{B 4}$$

The expansions U_1, U_2, V_1, V_2, $\bar{U}_1$, $\bar{U}_2$, $\bar{V}_1$ and $\bar{V}_2$ depend only on B and obey the following differential equations and interfacial conditions:

$$\nabla^2 U_1 = 1, \quad \nabla U_1 \cdot \boldsymbol{n} = 0, \tag{B 5a,b}$$

$$\nabla^2 \bar{U}_1 = 0, \quad \bar{U}_1 = U_1, \tag{B 6a,b}$$

$$\nabla^2 U_2 = 0, \quad \nabla U_2 \cdot \boldsymbol{n} = \nabla \bar{U}_1 \cdot \boldsymbol{n}, \tag{B 7a,b}$$

$$\nabla^2 \bar{U}_2 = 0, \quad \bar{U}_2 = U_2, \tag{B 8a,b}$$

$$\nabla^2 \bar{V}_1 = 1, \quad \bar{V}_1 = 0, \tag{B 9a,b}$$

$$\nabla^2 V_1 = 1, \quad \nabla V_1 \cdot \boldsymbol{n} = \nabla \bar{V}_1 \cdot \boldsymbol{n}, \tag{B 10a,b}$$

$$\nabla^2 \bar{V}_2 = 0, \quad \bar{V}_2 = V_1, \tag{B 11a,b}$$

$$\nabla^2 V_2 = 0, \quad \nabla V_2 \cdot \boldsymbol{n} = \nabla \bar{V}_2 \cdot \boldsymbol{n}. \tag{B 12a,b}$$

Further, the expansions also satisfy the no-slip condition at the wall and zero normal gradient at the symmetry boundaries. The above equations can be separated into two decoupled systems of equations: (B 5)–(B 8) and (B 9)–(B 12). Each system is solved sequentially using a numerical method similar to the one described in § A.1. Contours of the velocity expansions U_1, U_2, V_1, V_2, $\bar{U}_1$, $\bar{U}_2$, $\bar{V}_1$ and $\bar{V}_2$ in a square microchannel are shown in figure 14.

B.2. *Explanation of the velocity contours*

The first system of equations (B 5)–(B 8) shows that the leading-order corner flow U_1 is driven by a unit source and sees zero shear stress at the corner interface (figure 14*a*). This corner flow moves in the same direction as the drop and drags a drop flow $\bar{U}_1$ through the kinematic boundary condition (B 6*b*) at the corner interface (figure 14*c*). This dragged drop flow, therefore, is fastest at the corner interface and slows progressively towards the drop centre. This dragged drop flow $\bar{U}_1$ then induces a corner flow U_2 through the shear-stress balance (B 7*b*) at the corner interface (figure 14*b*). Since $\bar{U}_1$ is fastest at the interface, the shear stress at the interface induces U_2 to move in the opposite direction to $\bar{U}_1$ (except in a small region near the contact line, as shown by the velocity contours in figure 14*b*). The corner flow
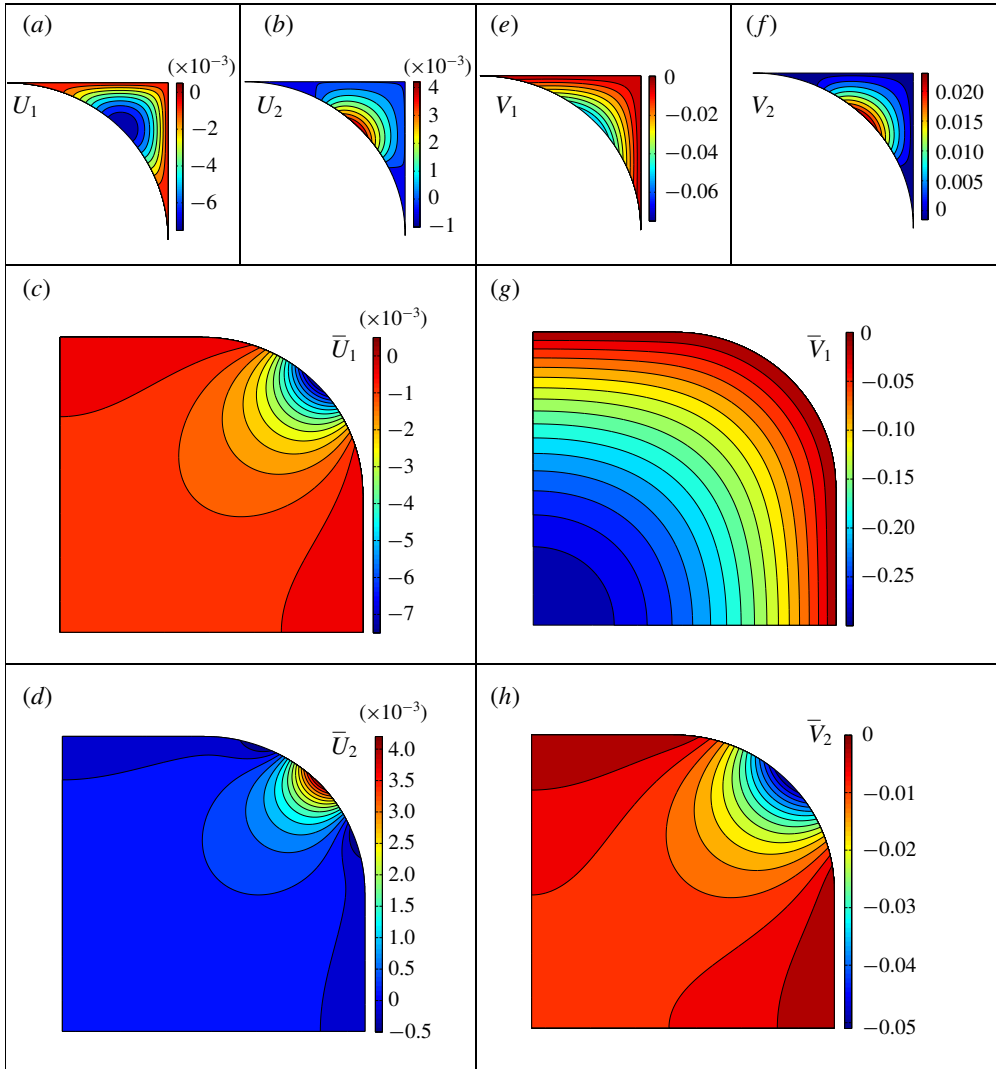
FIGURE 14. (Colour online) Contours of the velocity asymptotic expansions U_1 (*a*), U_2 (*b*), $\bar{U}_1$ (*c*), $\bar{U}_2$ (*d*), V_1 (*e*), V_2 (*f*), $\bar{V}_1$ (*g*), and $\bar{V}_2$ (*h*) in a square microchannel. The asymptotic expansions are defined in (B 1)–(B 4). Negative values indicate flowing in the same direction as the drop.

U_2 subsequently generates a drop flow $\bar{U}_2$ through the kinematic boundary condition (B 8*b*) at the corner interface (figure 14*d*). Thus, both U_2 and $\bar{U}_2$ are positive for most of the flow domain, whereas U_1 and $\bar{U}_1$ are everywhere negative. Hence, the first-order effect of drop viscosity (λ) is to reduce U_D and $\bar{U}_D$.

The second system of equations (B 9)–(B 12) shows that the leading-order drop and corner flows $\bar{V}_1$ and V_1 are both driven by a unit source. The drop flow $\bar{V}_1$ shown in figure 14(*g*) moves in the same direction as the drop and satisfies the no-slip condition at the corner interface according to (B 9*b*). The corner flow V_1 in figure 14(*e*) also moves in the direction of the drop. From (B 10), V_1 is driven by both the unit source and the shear stress at the corner interface exerted by $\bar{V}_1$. This corner

Coefficients	Aspect ratio			
$(\times 10^{-3})$	$B = 1.0$	$B = 1.2$	$B = 1.5$	$B = 2.0$
Q_{D1}	-0.7422	-1.049	-1.523	-2.280
Q_{D2}	0.2094	0.2959	0.4295	0.6416
Q_{P1}	-4.046	-5.692	-8.133	-11.79
Q_{P2}	1.383	1.945	2.776	4.011
$\bar{Q}_{D1}$	-3.303	-4.643	-6.609	-9.514
$\bar{Q}_{D2}$	1.174	1.650	2.347	3.369
$\bar{Q}_{P1}$	-534.8	-758.9	-1121	-1754
$\bar{Q}_{P2}$	-30.59	-42.78	-59.80	-83.07

TABLE 5. Numerical solution of the asymptotic expansions Q_{D1}, Q_{D2}, Q_{P1}, Q_{P2}, $\bar{Q}_{D1}$, $\bar{Q}_{D2}$, $\bar{Q}_{P1}$ and $\bar{Q}_{P2}$ of the volume-flow-rate coefficients defined in (B 17)–(B 20) for different aspect ratio B.

flow V_1 then drags a drop flow $\bar{V}_2$ through the kinematic boundary condition (B 11*b*) at the corner interface (figure 14*h*). Thus, $\bar{V}_2$ moves in the same direction as V_1, is fastest at the corner interface, and slows towards the drop centre. Its shear stress at the corner interface points in the opposite direction to $\bar{V}_2$ and induces through the shear-stress balance (B 12*b*) a corner flow V_2 (figure 14*f*). Thus, V_2 moves in the opposite direction to $\bar{V}_2$ or V_1. Hence, the first-order effect of drop viscosity (λ) is to reduce U_P and enhance $\bar{U}_P$.

B.3. *Volume-flow-rate coefficients*

The asymptotic expansions of U_D, U_P, $\bar{U}_D$ and $\bar{U}_P$ in (B 1)–(B 4) are substituted into (4.8*b,c*) and (4.10*b,c*) to yield

$$\bar{Q}_D = \bar{Q}_{D1} + \lambda \bar{Q}_{D2}, \tag{B 13}$$

$$\bar{Q}_P = \bar{Q}_{P1} + \lambda \bar{Q}_{P2}, \tag{B 14}$$

$$Q_D = Q_{D1} + \lambda Q_{D2}, \tag{B 15}$$

$$Q_P = Q_{P1} + \lambda Q_{P2}, \tag{B 16}$$

where

$$\bar{Q}_{D1} = \iint_{\bar{A}} \bar{U}_1 \, \mathrm{d}y \, \mathrm{d}z, \quad \bar{Q}_{D2} = \iint_{\bar{A}} \bar{U}_2 \, \mathrm{d}y \, \mathrm{d}z, \tag{B 17a,b}$$

$$\bar{Q}_{P1} = \iint_{\bar{A}} \bar{V}_1 \, \mathrm{d}y \, \mathrm{d}z, \quad \bar{Q}_{P2} = \iint_{\bar{A}} \bar{V}_2 \, \mathrm{d}y \, \mathrm{d}z, \tag{B 18a,b}$$

$$Q_{D1} = \iint_{A} U_1 \, \mathrm{d}y \, \mathrm{d}z, \quad Q_{D2} = \iint_{A} U_2 \, \mathrm{d}y \, \mathrm{d}z, \tag{B 19a,b}$$

$$Q_{P1} = \iint_{A} V_1 \, \mathrm{d}y \, \mathrm{d}z, \quad Q_{P2} = \iint_{A} V_2 \, \mathrm{d}y \, \mathrm{d}z. \tag{B 20a,b}$$

These volume-flow-rate coefficients are determined numerically following the method described in § A.1. The expansions depend only on the aspect ratio B and are listed in table 5 for $B = 1$, 1.2, 1.5, and 2. The asymptotic solutions are also plotted in figure 4, which shows that they are accurate for $0 \leqslant \lambda < 0.2$. The comparison validates both the numerical solutions and the asymptotic expansions. The asymptotic solutions reveal the first-order effects of λ on the volume-flow-rate coefficients.
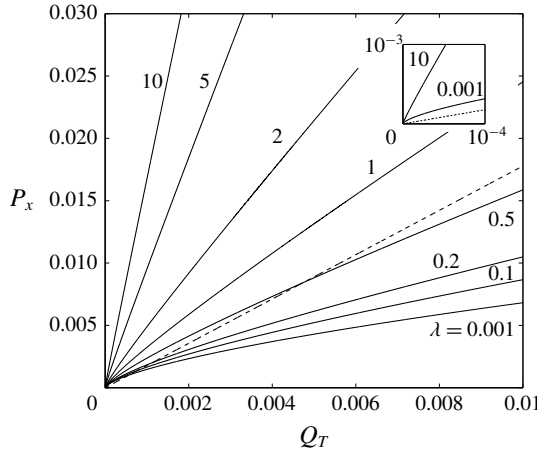
FIGURE 15. Pressure-flow rate relation for drop flow in a square microchannel for $L = 10$ and various λ. The insert shows an expanded view near $Q_T = 0$. The dashed line is for the single-phase carrier-liquid flow.

Appendix C. Pressure-flow rate relation: $P_x = P_x(Q_T)$

Elimination of Ca from equations (4.12a) and (4.16a) gives

$$P_x^3 + hP_x^2 + rP_x + s = 0, \tag{C 1a}$$

where

$$h = \frac{(q_D k_U - q_U k_D)q_D^2}{L^3 q_U^3} - \frac{3k_U}{q_U}Q_T, \tag{C 1b}$$

$$r = \frac{2q_D(q_U k_D - q_D k_U)k_D}{L^3 q_U^3}Q_T + \frac{3k_U^2}{q_U^2}Q_T^2, \tag{C 1c}$$

$$s = \frac{k_D^2(q_D k_U - q_U k_D)}{L^3 q_U^3}Q_T^2 - \frac{k_U^3}{q_U^3}Q_T^3. \tag{C 1d}$$

The only real root of (C 1a) is

$$P_x = \frac{1}{3}\left(c + \frac{h^2 - 3r}{c} - h\right), \tag{C 2a}$$

where

$$c = \left\{\tfrac{1}{2}[3\sqrt{3}(27s^2 + 4h^3 s + 4r^3 - 18hrs - h^2 r^2)^{1/2} + 9hr - 2h^3 - 27s]\right\}^{1/3}. \tag{C 2b}$$

Figure 15 shows the pressure-flow rate relation in (C 2) for $L = 10$, $B = 1$, and various λ. The dotted line represents the pressure-flow rate relation for single-phase flow of the carrier liquid. As $Q_T \to 0$, the pressure gradient required to drive drop flow is always higher than that required to drive single-phase flow, as seen in the insert in figure 15. As Q_T increases, the pressure gradient required to drive drop flow may be higher or lower than that for single-phase flow depending on λ, as seen in figure 15.

REFERENCES

ANNA, S. L. 2016 Droplets and bubbles in microfluidic devices. *Annu. Rev. Fluid Mech.* **48** (1), 285–309.

BAROUD, C. N., GALLAIRE, G. & DANGLA, R. 2010 Dynamics of microfluidic droplets. *Lab on a Chip* **10**, 2032–2045.

CHAUDHURY, K., ACHARYA, P. V. & CHAKRABORTY, S. 2014 Influence of disjoining pressure on the dynamics of steadily moving long bubbles inside narrow cylindrical capillaries. *Phys. Rev.* E **89** (5), 053002.

CHEN, H., LI, Z. & LI, J. 2016 Thin-film profile around long bubbles in square microchannels measured by chromatic interference method. *Appl. Phys. Lett.* **109**, 041604.

CHERLO, S. K. R., KARIVETI, S. & PUSHPAVANAM, S. 2010 Experimental and numerical investigations of two-phase (liquid–liquid) flow behavior in rectangular microchannels. *Ind. Engng Chem. Res.* **49** (2), 893–899.

DAVIS, S. H. 1980 Moving contact lines and rivulet instabilities. Part 1. The static rivulet. *J. Fluid Mech.* **98** (2), 225–242.

FUERSTMAN, M. J., LAI, A., THURLOW, M. E., SHEVKOPLYAS, S. S., STONE, H. A. & WHITESIDES, G. M. 2007 The pressure drop along rectangular microchannels containing bubbles. *Lab on a Chip* **7** (11), 1479–1489.

HAMMOUD, N. H., TRINH, P. H., HOWELL, P. D. & STONE, H. A. 2017 Influence of van der Waals forces on a bubble moving in a tube. *Phys. Rev. Fluids* **2** (6), 063601.

HOANG, D. A., VAN STEIJN, V., PORTELA, L. M., KREUTZER, M. T. & KLEIJN, C. R. 2013 Benchmark numerical simulations of segmented two-phase flows in microchannels using the volume of fluid method. *Comput. Fluids* **86**, 28–36.

HODGES, S. R., JENSEN, O. E. & RALLISON, J. M. 2004 The motion of a viscous drop through a cylindrical tube. *J. Fluid Mech.* **501**, 279–301.

HUEBNER, A., SHARMA, S., SRISA-ART, M., HOLLFELDER, F., EDEL, J. B. & DEMELLO, A. J. 2008 Microdroplets: a sea of applications? *Lab on a Chip* **8** (8), 1244–1254.

JAKIELA, S., KORCZYK, P. M., MAKULSKA, S., CYBULSKI, O. & GARSTECKI, P. 2012 Discontinuous transition in a laminar fluid flow: a change of flow topology inside a droplet moving in a micron-size channel. *Phys. Rev. Lett.* **108** (13), 134501.

JAKIELA, S., MAKULSKA, S., KORCZYK, P. M. & GARSTECKI, P. 2011 Speed of flow of individual droplets in microfluidic channels as a function of the capillary number, volume of droplets and contrast of viscosities. *Lab on a Chip* **11** (21), 3603–3608.

JIN, Y., ORTH, A., SCHONBRUN, E. & CROZIER, K. B. 2012 Measuring the pressures across microfluidic droplets with an optical tweezer. *Opt. Exp.* **20** (22), 24450–24464.

JOVANOVIĆ, J., REBROV, E. V., NIJHUIS, T. A., HESSEL, V. & SCHOUTEN, J. C. 2010 Phase-transfer catalysis in segmented flow in a microchannel: fluidic control of selectivity and productivity. *Ind. Engng Chem. Res.* **49** (6), 2681–2687.

JOVANOVIĆ, J., ZHOU, W., REBROV, E. V., NIJHUIS, T. A., HESSEL, V. & SCHOUTEN, J. C. 2011 Liquid–liquid slug flow: hydrodynamics and pressure drop. *Chem. Engng Sci.* **66** (1), 42–54.

KIM, N., MURPHY, M. C., SOPER, S. A. & NIKITOPOULOS, D. E. 2014 Liquid–liquid segmented flows in polycarbonate microchannels with cross-sectional expansions. *Intl J. Multiphase Flow* **58** (0), 83–96.

KINOSHITA, H., KANEDA, S., FUJII, T. & OSHIMA, M. 2007 Three-dimensional measurement and visualization of internal flow of a moving droplet using confocal micro-PIV. *Lab on a Chip* **7**, 338–346.

LAC, E. & SHERWOOD, J. D. 2009 Motion of a drop along the centreline of a capillary in a pressure-driven flow. *J. Fluid Mech.* **640**, 27–54.

MATHWORKS 2017 *Partial Differential Equation Toolbox: User's Guide* (R2013b). Retrieved December 17. http://www.mathworks.com/help/pdf_doc/pde/pde.pdf.

PARK, C.-W. & HOMSY, G. 1984 Two-phase displacement in Hele Shaw cells: theory. *J. Fluid Mech.* **139** (1), 291–308.

PATZEK, T. W. & KRISTENSEN, J. G. 2001 Shape factor correlations of hydraulic conductance in noncircular capillaries: II. Two-phase creeping flow. *J. Colloid Interface Sci.* **236** (2), 305–317.

RAJ, R., MATHUR, N. & BUWA, V. V. 2010 Numerical simulations of liquid–liquid flows in microchannels. *Ind. Engng Chem. Res.* **49** (21), 10606–10614.

RANSOHOFF, T. C. & RADKE, C. J. 1988 Laminar flow of a wetting liquid along the corners of a predominantly gas-occupied noncircular pore. *J. Colloid Interface Sci.* **121** (2), 392–401.

RAO, S. S. 2015 Modeling two-phase flow and heat transfer in polygonal microchannels. Doctoral dissertation, Louisiana State University, LA. https://digitalcommons.lsu.edu/gradschool_dissertations/1087.

RAO, S. S. & WONG, H. 2015 Heat and mass transfer in polygonal micro heat pipes under small imposed temperature differences. *Intl J. Heat Mass Transfer* **89**, 1369–1385.

SARRAZIN, F., BONOMETTI, T., PRAT, L., GOURDON, C. & MAGNAUDET, J. 2008 Hydrodynamic structures of droplets engineered in rectangular micro-channels. *Microfluid. Nanofluid.* **5** (1), 131–137.

SARRAZIN, F., LOUBIÈRE, K., PRAT, L., GOURDON, C., BONOMETTI, T. & MAGNAUDET, J. 2006 Experimental and numerical study of droplets hydrodynamics in microchannels. *AIChE J.* **52** (12), 4061–4070.

SHIKHMURZAEV, Y. D. 1997 Moving contact lines in liquid/liquid/solid systems. *J Fluid Mech.* **334**, 211–249.

SNOEIJER, J. H. & ANDREOTTI, B. 2013 Moving contact lines: scales, regimes, and dynamical transitions. *Annu. Rev. Fluid Mech.* **45**, 269–292.

SOARES, E. J. & THOMPSON, R. L. 2009 Flow regimes for the immiscible liquid–liquid displacement in capillary tubes with complete wetting of the displaced liquid. *J. Fluid Mech.* **641**, 63–84.

SONG, H., CHEN, D. L. & ISMAGILOV, R. F. 2006 Reactions in droplets in microfluidic channels. *Angew. Chem. Intl Ed. Engl.* **45** (44), 7336–7356.

STONE, H. A., STROOCK, A. D. & AJDARI, A. 2004 Engineering flows in small devices. *Annu. Rev. Fluid Mech.* **36** (1), 381–411.

TAN, J., XU, J. H., LI, S. W. & LUO, G. S. 2008 Drop dispenser in a cross-junction microfluidic device: scaling and mechanism of break-up. *Chem. Engng J.* **136** (2), 306–311.

TEH, S.-Y., LIN, R., HUNG, L.-H. & LEE, A. P. 2008 Droplet microfluidics. *Lab on a Chip* **8** (2), 198–220.

THOMPSON, P. A. & TROIAN, S. M. 1997 A general boundary condition for liquid flow at solid surfaces. *Nature* **389**, 360–362.

VANAPALLI, S. A., BANPURKAR, A. G., VAN DEN ENDE, D., DUITS, M. H. G. & MUGELE, F. 2009 Hydrodynamic resistance of single confined moving drops in rectangular microchannels. *Lab on a Chip* **9** (7), 982–990.

VLADIMIR, S. A. & HOMSY, G. M. 2006 Modeling shapes and dynamics of confined bubbles. *Annu. Rev. Fluid Mech.* **38** (1), 277–307.

WHITE, F. M. 1991 *Viscous Fluid Flow*, 2nd edn., p. 120. McGraw-Hill.

WONG, H., FATT, I. & RADKE, C. J. 1996 Deposition and thinning of the human tear film. *J. Colloid Interface Sci.* **184** (1), 44–51.

WONG, H., MORRIS, S. & RADKE, C. J. 1992 Three-dimensional menisci in polygonal capillaries. *J. Colloid Interface Sci.* **148** (2), 317–336.

WONG, H., RADKE, C. J. & MORRIS, S. 1995a The motion of long bubbles in polygonal capillaries. Part 1. Thin films. *J. Fluid Mech.* **292**, 71–94.

WONG, H., RADKE, C. & MORRIS, S. 1995b The motion of long bubbles in polygonal capillaries. II: drag, fluid pressure and fluid flow. *J. Fluid Mech.* **292**, 95–110.

YONG, Y., YANG, C., JIANG, YI., JOSHI, A., SHI, Y. & YIN, X. 2011 Numerical simulation of immiscible liquid–liquid flow in microchannels using lattice Boltzmann method. *Sci. China Chem.* **54** (1), 244–256.